JGR Solid Earth

RESEARCH ARTICLE
10.1029/2020JB020503

Key Points:
- Slow slip events >M_w 6.6 in northwestern Costa Rica occurred every 21.7 ± 2.6 months based on data from 33 GPS stations between 2002 to 2020
- Slow slip recurrence/distribution and inter-transient strain accumulation patterns were unchanged by the 5 September 2012 M_w 7.6 earthquake
- Some inter-transient locked patches offshore did not rupture in 2012 and do not participate in slow slip events

Supporting Information:
- Supporting Information S1
- Movie S1
- Movie S2
- Movie S3
- Movie S4
- Movie S5
- Movie S6
- Movie S7
- Movie S8

Correspondence to:
S. Xie,
suruixie@usf.edu

Citation:
Xie, S., Dixon, T. H., Malservisi, R., Jiang, Y., Protti, M., & Muller, C. (2020). Slow slip and Inter-transient locking on the Nicoya megathrust in the late and early stages of an earthquake cycle. *Journal of Geophysical Research: Solid Earth*, *125*, e2020JB020503. https://doi.org/10.1029/2020JB020503

Received 7 JUL 2020
Accepted 19 OCT 2020
Accepted article online 20 OCT 2020

Slow Slip and Inter-transient Locking on the Nicoya Megathrust in the Late and Early Stages of an Earthquake Cycle

Surui Xie[1,2], Timothy H. Dixon[1], Rocco Malservisi[1], Yan Jiang[3,4], Marino Protti[5], and Cyril Muller[5]

[1]School of Geosciences, University of South Florida, Tampa, FL, USA, [2]Scripps Institution of Oceanography, University of California, San Diego, La Jolla, CA, USA, [3]Geological Survey of Canada, Natural Resources Canada, Sidney, Canada, [4]School of Earth and Ocean Sciences, University of Victoria, Victoria, Canada, [5]Observatorio Vulcanológico y Sismológico de Costa Rica, Universidad Nacional, Heredia, Costa Rica

Abstract We analyzed continuous GPS data collected from 2002–2020 to characterize slow slip events (SSEs) in and near the Nicoya Peninsula, Costa Rica. These data are bisected by the 5 September 2012 M_w 7.6 earthquake. The displacement time series contain multiple signals, including plate convergence, plate interface locking, coseismic and postseismic deformation, seasonal oscillations, SSEs, and noise. GPS-measured coseismic and postseismic displacements associated with the M_w 7.6 earthquake are modeled and removed by a step function plus multiple timescale relaxation processes with four characteristic times: 11, 94, 470, and 1,865 days. Seasonal oscillations are eliminated using a multichannel singular spectrum analysis (M-SSA). Ten major SSEs (M_w > 6.6) are observed in the remaining time series, with a constant recurrence interval of 21.7 ± 2.6 months. SSEs occur in both shallow (~10 km) and deep (~35 km) portions of the plate interface, but the latter last longer and have larger magnitudes. There is minimum to no slow slip in the M_w 7.6 seismic rupture area and a persistent slow slip patch beneath the Nicoya Gulf entrance. Despite strong earthquake-related stress perturbations, the inter-SSE locking status on the megathrust is very similar between the late and early stages of the earthquake cycle and includes locked patches that ruptured in the 2012 earthquake or continue to rupture via SSEs. Some locked patches offshore south of the Nicoya Peninsula did not rupture in 2012, do not participate in SSEs, and may be indicative of supercycle behavior, that is, strain accumulation over several seismic cycles. These areas warrant heightened monitoring.

Plain Language Summary Slow slip events (SSEs) release strain energy in Earth's crust that accumulates due to plate motion and frictional locking on the boundaries between plates. SSEs are similar to earthquakes but are less damaging, since strain is released slowly, over weeks or months. We used GPS measurements with millimeter precision to study SSEs in Northwestern Costa Rica between 2002 and 2020 and compared them to the pattern of strain accumulation over the same period. We find that these events happened about every 22 months, and the repeat time is unchanged by the 5 September 2012 M_w 7.6 Costa Rica earthquake. Locking patterns also remain similar before and after this earthquake. However, some locked zones did not rupture in the 2012 earthquake or earthquakes in the last few decades and do not participate in SSEs. These areas may represent zones of higher seismic risk in the future.

1. Introduction

In subduction plate boundaries, where one plate slides beneath another, large earthquakes and occasional tsunamis have occurred in the past and will strike the same regions again in the future, posing threats to society. Observation and modeling of strain accumulation and release processes here can be used to characterize and potentially forecast future damaging events in these regions. Slow slip events (SSEs) represent a distinct strain release process that occurs in many subduction zones (e.g., Douglas et al., 2005; Dragert et al., 2001; Larson et al., 2004; Obara et al., 2004; Ohta et al., 2006; Outerbridge et al., 2010). Some studies suggest that SSEs release a significant amount of accumulated strain during the interseismic period, perhaps limiting future major earthquake magnitude and tsunami potential (e.g., Dixon et al., 2014; Rolandone et al., 2018). Other work suggests that SSEs can cause stress perturbations on adjacent fault segments,

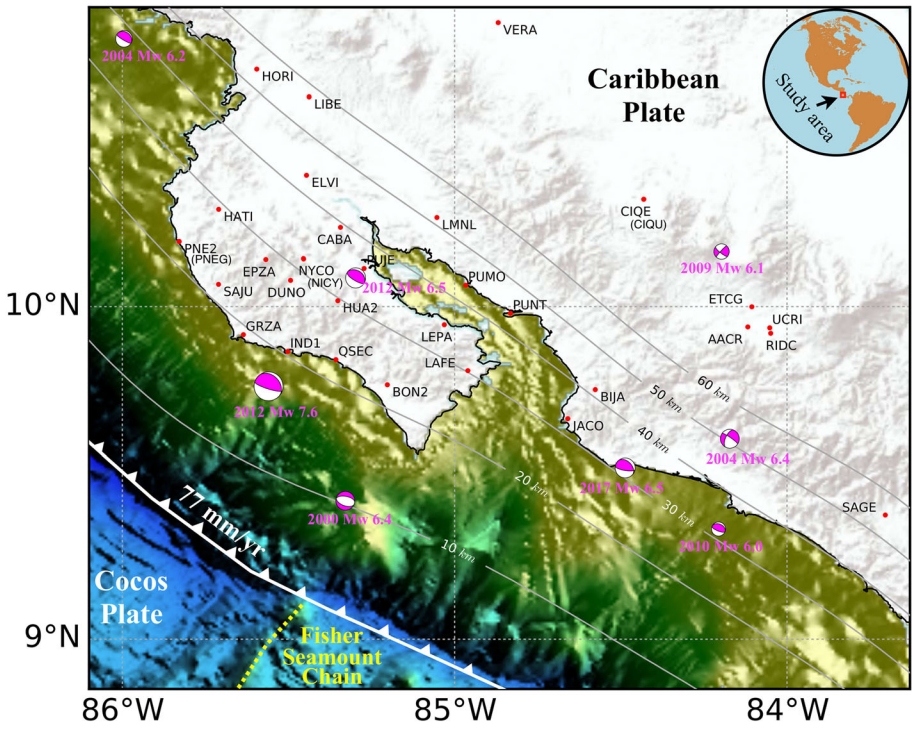

Figure 1. Continuous GPS network in northwestern Costa Rica. Red dots show station locations, with four-character station IDs labeled. CIQE, NYCO, and PNE2 are located near decommissioned stations CIQU, NICY, and PNEG, respectively. Gray contours represent the dipping plate interface depths (Hayes et al., 2018). Thick white line marks approximate location of the trench. Plate rate of Cocos relative to Caribbean is calculated with the MORVEL plate motion model (DeMets et al., 2010). Magenta-white beach balls show locations of $M_w \geq 6.0$ earthquakes that occurred from 2000 to 2020. Epicenter of the 2012 M_w 7.6 earthquake is from Yue et al. (2013); epicenters of the other earthquakes are from the USGS catalogue.

sometimes triggering devastating earthquakes (e.g., Uchida et al., 2016), or evolve into megathrust earthquakes (e.g., Segall & Bradley, 2012). Either way, precisely measuring and characterizing SSEs may help to define future earthquake rupture time and area and characterize and understand physical conditions on the seismogenic plate interface.

SSEs are largely aseismic events but often co-occur with nonvolcanic tremor (Dragert et al., 2001; Schwartz & Rokosky, 2007). They can have durations ranging from minutes to years (Bürgmann, 2018) but the majority last several weeks to several months. Although seismological observations can help constrain SSE occurrence, continuous geodetic observations (mainly Global Navigation Satellite System, GNSS) are perhaps the most reliable way to document SSEs and are routinely used for this purpose.

The Nicoya Peninsula of Costa Rica overlies part of the seismogenic zone in Central America, where the Cocos plate subducts northeastward beneath the Caribbean plate at a rate of ~77 mm/year (Figure 1), providing a good location to study subduction zone seismic processes. Earthquakes with moment magnitudes greater than 7 occur here approximately every 50–60 years. The most recent one ($M_w = 7.6$) occurred on 5 September 2012 (Protti et al., 2014). A network of continuous GNSS stations (Figure 1; unless noted only continuous GPS [cGPS] measurements are used in this study) initiated in 2002 has now recorded both the late and early stages of the earthquake cycle, facilitating detailed studies of several critical processes, including interseismic coupling (Feng et al., 2012), coseismic rupture (Protti et al., 2014; Yue et al., 2013), postseismic behavior (Hobbs et al., 2017; Malservisi et al., 2015), and slow slip events (Jiang et al., 2012; Outerbridge et al., 2010; Voss et al., 2017). Previous studies showed that SSEs in this area are temporally accompanied by seismic tremor (Jiang et al., 2012; Outerbridge et al., 2010), have an average recurrence interval of ~21 months (Jiang et al., 2012), lie off the main coseismic rupture area but over some inter-SSE locked patches (Dixon et al., 2014), and vary in magnitude and spatial distribution of slip (Jiang et al., 2012; Voss et al., 2017).

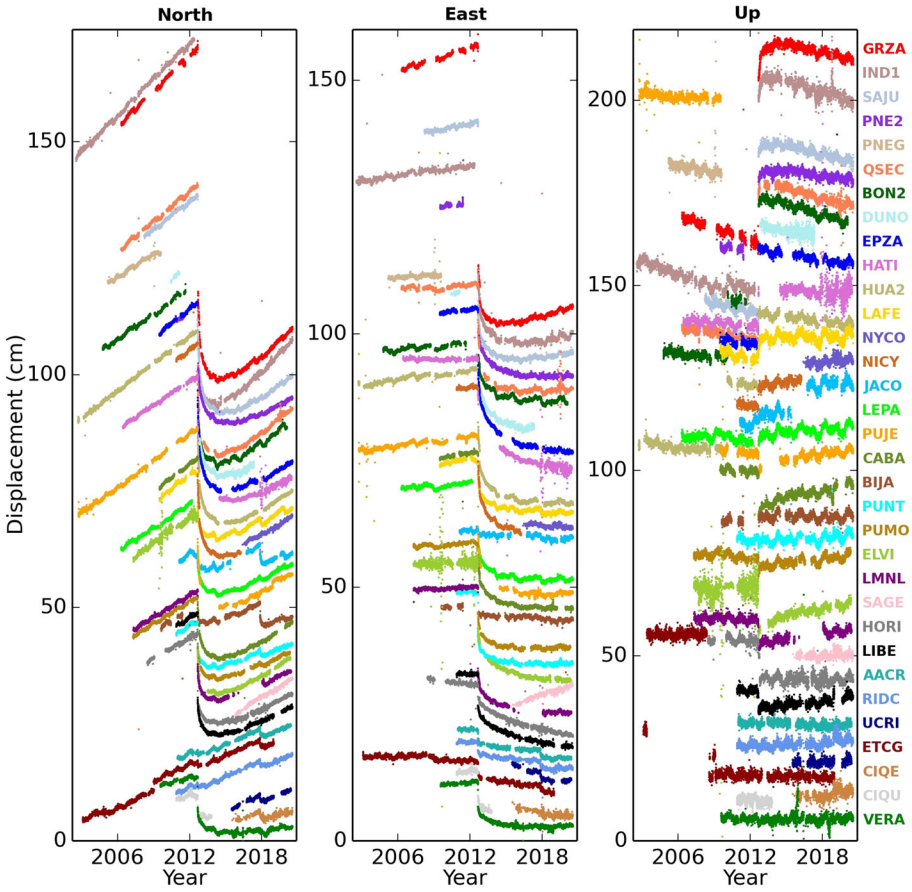

Figure 2. Raw GPS time series. Displacements are offset for clarity. Each color corresponds to one GPS station labeled on the right. GPS stations are arranged by the approximate slab depth from shallow to deep. The north component of station LEPA at expanded scale is presented in Figure 12a.

Here we report analyses of continuous GPS data obtained in and near the Nicoya Peninsula from 2002 to 2020. We aim to generate a consistent catalogue of SSEs and inter-SSE locking in the area and time frame spanning the 2012 M_w 7.6 earthquake. Several challenges exist (1) GPS measurements here have relatively large uncertainties compared to midlatitude regions, due mainly to variable atmospheric (mainly wet tropospheric) delay in this tropical environment; (2) seasonal variations in surface deformation are significant, primarily driven by the seasonal hydrological cycle; (3) GPS time series are bisected by the 2012 M_w 7.6 earthquake, which induces large and complicated postseismic motion. We therefore describe in some detail the methods we used to reduce the impact of these confounding effects and processes.

2. GPS Data Processing

Available data obtained by the cGPS network from July 2002 to July 2020 were analyzed into daily averaged positions. Data processing was done with the precise point positioning method (Zumberge et al., 1997) using GipsyX software (v.1.4), with orbit and satellite clock estimates provided by the Jet Propulsion Laboratory. Ocean tide loading corrections were computed on the Onsala Space Observatory website (http://holt.oso.chalmers.se/loading/) with the FES2004 model (Lyard et al., 2006). Tropospheric delays were estimated using the VMF1 mapping function (Böhm et al., 2006). Second-order ionospheric effects were corrected using the IONEX model (Kedar et al., 2003). Initial daily solutions were aligned with the IGS14 reference frame (Rebischung et al., 2016). Resultant GPS time series are shown in Figure 2. To investigate site velocities relative to the stable Caribbean plate, solutions were transformed into the regional reference frame CARIB18 (Wang et al., 2019).

3. GPS Time Series Analysis

The GPS displacement time series reflect a large number of processes. Providing the impact of those processes that are considered noise can be reduced or eliminated, the residual displacement data contain rich information on interseismic plate motion and locking, seasonal ground motion, coseismic and postseismic deformation, and slow slip events. These various processes can be described by the equation:

$$\begin{aligned} x(t_i) \quad &= a + bt_i + c\sin(2\pi t_i) + d\cos(2\pi t_i) + f\sin(4\pi t_i) + g\cos(4\pi t_i) + \\ &\sum_{h=1}^{l} D_h \mathrm{H}(t_i - t_h) + \sum_{p=1}^{m} D_p \mathrm{H}(t_i - T_{eq})\left(1 - e^{-\frac{t_i - T_{eq}}{\tau_p}}\right) + \\ &\sum_{s=1}^{n} D_s \mathrm{F}_s(t_i) + v_i \end{aligned} \tag{1}$$

where $x(t_i)$ is the position of a GPS station at time t_i, a is the intercept, b is the secular rate, and c, d, f, and g represent the amplitudes and phases of the annual and semiannual variations. Accordingly, the unit of t_i must be years if Equation 1 is used to fit these seasonal terms. D_h is the hth offset caused by a GPS antenna change or an earthquake at time t_h, represented by a Heaviside function H $(t_i - t_h)$. D_p and τ_p correspond to the amplitude and characteristic relaxation time of the pth component of the postseismic deformation after the 2012 M_w 7.6 earthquake that occurred at time T_{eq}. D_s and F_s (t_i) represent the displacement and characteristic function of the sth slow slip event. v_i denotes noise.

To identify and model slow slip events from GPS time series, we first eliminated signals associated with antenna changes, secular motion and the 2012 M_w 7.6 earthquake, which are the predominant signals. This helps to highlight the remaining signals, which otherwise would be dwarfed. Next, we used the multichannel singular spectrum analysis (M-SSA) method (Walwer et al., 2016) to remove seasonal oscillations, which can have similar amplitudes to SSE displacements. Remaining time series are detrended, leaving SSE-associated displacements for further analysis.

3.1. Removal of Coseismic and Postseismic Processes in the GPS Time Series

Four $M_w > 6.2$ earthquakes struck the study area during the study period: a M_w 6.4 earthquake on 20 November 2004, a M_w 7.6 earthquake on 5 September 2012, a M_w 6.5 earthquake on 24 October 2012, and a M_w 6.5 earthquake on 12 November 2017 (Figure 1). Among them, the M_w 7.6 earthquake caused distinct coseismic and postseismic displacements on all GPS stations (Figure 2). Malservisi et al. (2015) analyzed cGPS data collected within the first 2 years after the 2012 M_w 7.6 earthquake, suggesting that the postseismic behavior could be described with three characteristic relaxation times: 7, 70, and more than 400 days. Following their method but with postearthquake data spanning longer than 7 years, we searched for the minimum number of characteristic relaxation times needed to represent the postseismic displacements in the GPS time series, that is, parameter m in Equation 1. Since many GPS stations have large data gaps, we chose five stations (IND1, SAJU, EPZA, HUA2, and CABA) with relatively long time series for the postseismic characteristic time estimates. These five stations all have more than 3 years of data before the 2012 M_w 7.6 earthquake, allowing robust estimates of secular rate. They also all have data collected within the first week of the main shock and were still operating in 2020, allowing a wide range of characteristic times to be constrained. Using an F test, we found that four characteristic times fit the GPS time series quite well: 11, 94, 470, and 1,865 days. More than four characteristic times does not improve data fit at the 95% confidence level. While these characteristic times do not necessarily correspond to actual physical processes, it is likely that the shorter characteristic times mainly reflect after-slip and poro-elastic response in the upper crust, while the longer characteristic times mainly reflect viscoelastic relaxation of the lower crust and upper mantle (Malservisi et al., 2015; McCormack et al., 2020). Note that the details of these characteristic times and the removal of their influence from the time series is not critical for SSE identification; SSEs can be observed in some of the raw time series (e.g., north component of stations LAFE and LEPA; Figure 2). However, accounting for the various postseismic processes improves estimation of SSE timing and amplitude, especially for stations with smaller SSE displacements.

A Heaviside function and the estimated four characteristic times were used to model and remove the coseismic and postseismic displacements caused by the 2012 M_w 7.6 earthquake. The 2004 M_w 6.4 earthquake and

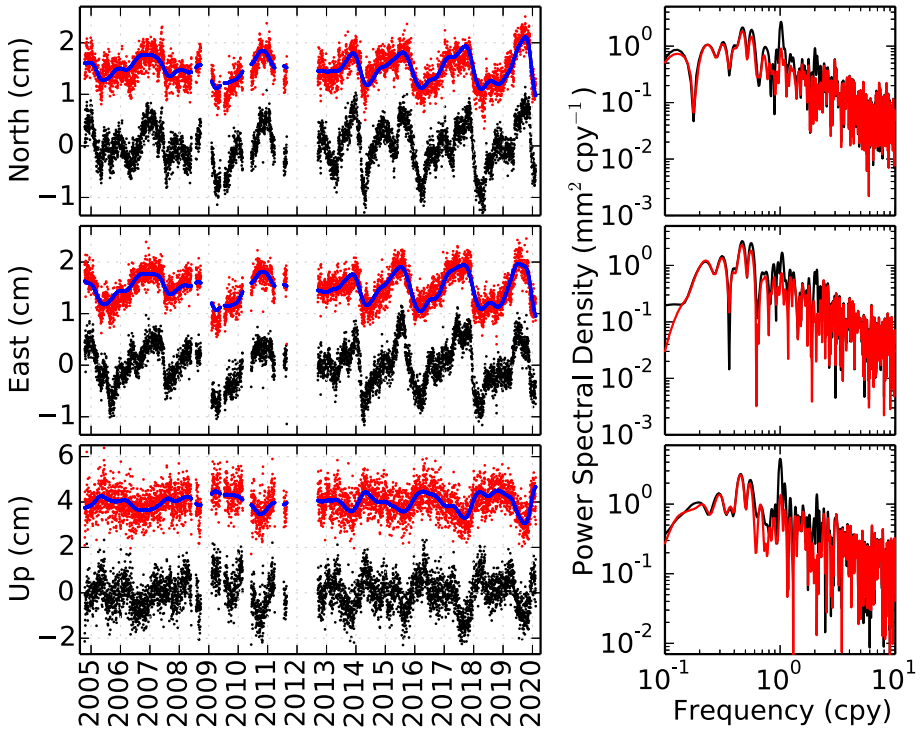

Figure 3. Example of seasonal oscillation removal. (left) Detrended time series for station BON2. Black dots show displacements without seasonal oscillation removal. Red dots show displacements with annual and semiannual signals removed and are offset for clarity. Blue lines show reconstructed time series using the highest 12 ranking principal components (annual and semiannual signals removed) from the M-SSA analysis. (right) Power spectral density plots of the raw (black) and annual and semiannual signals removed (red) time series. Note changes at 1 and 2 cycle-per-year frequencies.

the 2012 M_w 6.5 earthquake signals were removed using Heaviside functions. If there is any postseismic displacement associated with the 2012 M_w 6.5 earthquake, it should be largely subtracted by the postseismic decay functions for the 2012 M_w 7.6 earthquake. The 2017 M_w 6.5 earthquake occurred near the beginning of a SSE (see below), with several stations east of the Nicoya Peninsula showing significant coseismic displacements (e.g., BIJA and JACO). However, most other stations do not have apparent displacements associated with this earthquake, making it difficult to separate signals of seismic deformation and the SSE. Here we do not attempt to eliminate the influence of the 2017 M_w 6.5 earthquake. Instead, we modeled the earthquake and coincident SSE as a single event. To model stations east of the Nicoya Peninsula, data within 200 days after the 2017 M_w 6.5 earthquake were not used and a Heaviside function was used to account for displacements caused by this earthquake. Black dots on the left column of Figure 3 show an example of the remodeled time series for station BON2.

3.2. Seasonal Oscillation Removal From the GPS Time Series

Due to Earth surface mass (mainly hydrologic) redistribution and other seasonally varying processes, GPS positions can exhibit significant seasonal variations (Dong et al., 2002). In and near the Nicoya Peninsula, the amplitudes of seasonal variations in GPS position time series can approach the level of SSE signals, making it difficult to identify small SSE signals. A common method to reduce the influence of seasonal variations is to use sine and cosine functions to model the annual and semiannual signals (e.g., Jiang et al., 2012). This method assumes fixed amplitudes and phases for the seasonal variations. More recently, new approaches have been developed to allow estimation of seasonal signals with varying amplitudes and phases, such as M-SSA (Walwer et al., 2016). Voss et al. (2017) applied the M-SSA approach to GPS time series in the Nicoya Peninsula and showed promising improvement in separation of seasonal oscillations from SSE signals. We used the same method but made several changes. First, we used a time lag of 850 days instead of 660 days in forming the data matrix. This ensures the time lag is longer than the longest interval between SSEs. Second, instead of estimating the seasonal oscillations over the entire network (i.e., use all

three components of all GPS stations in creating the data matrix), we estimated the seasonal oscillations at each station independently using the three components (North/East/Up) as three channels. This is because the number of operational GPS stations in the network varies significantly during the study period. A network-wide data matrix in M-SSA analysis would require interpolating large amounts of missing data (Walwer et al., 2016). Thus, seasonal oscillations in the early period of the network (before 2007) cannot be robustly estimated due to lack of seasonal variations in the interpolated data. A test run with a network-wide M-SSA analysis shows nearly identical results for data obtained after 2007. Prior to 2007, the extracted seasonal signals for network-wide M-SSA analysis are much smaller than the apparent seasonal variations, at the level of the interpolated Gaussian random variables for the not-yet-operating stations. In contrast, for the individual station M-SSA analysis, the estimated seasonal oscillations represent the data well.

Figure 3 shows an example of seasonal oscillation removal with the M-SSA approach. Black dots on the left column show detrended time series that include seasonal oscillations. Red dots show annual and semiannual variation removed with the M-SSA analysis. Blue curves show the reconstructed time series with the highest 12 ranking principal components (PCs) that exclude annual and semiannual components. The ranking is by eigenvalues from the highest to lowest. The annual and semiannual components are identified based on the power spectrum, shown on the right column of Figure 3. Significant reductions at 1 and 2 cycle-per-year frequencies but not at other frequencies suggest that seasonal variations in displacement time series are effectively reduced using the M-SSA approach.

Figure 4 shows seasonal oscillation-removed time series for all analyzed GPS stations, arranged along dip direction from shallow to deep. Several SSEs are visible, even in the vertical component (e.g., stations LAFE and LEPA, where reverse displacements occur every ~22 months), which is typically three times noisier than the horizontal components. Some previous SSE studies in this region did not use the vertical component due to high noise levels (e.g., Outerbridge et al., 2010). With the new noise reduction approach, we believe that the vertical component can provide useful constraints, hence it is included in our analysis.

The positionogram method uses color variations to represent transitions from inter-transient to transient motions and is a good way to illustrate SSE timing (e.g., Jiang et al., 2012). In theory, if seasonal variations, transients other than SSEs, and noise are completely eliminated, the only color changes reflect SSEs. Since SSEs may extend across several GPS site locations, assessing times when multiple nearby stations show similar color variations is an effective way to define the SSEs. Jiang et al. (2012) found good spatial and temporal correlations between different stations during SSEs. We adopted this method, but instead of using a cubic spline to smooth the time series, we used the reconstructed time series of the highest 12 ranking principal components from the M-SSA analysis. These 12 principal components contain minimum noise and nicely represent the time series after removal of seasonal oscillations (see example in Figure 3). The color scheme in Figure 5 shows the positionograms of the three components for all GPS stations, where blue to red transitions correspond to periods with positive velocities and red to blue transitions correspond to periods with negative velocities. Several clusters of transitions from red to blue in the horizontal components appear, indicating possible SSE displacements (reverse motion). Note that there is no obvious annual or semiannual variation in the positionograms, strong evidence that the seasonal oscillations were effectively removed by the M-SSA analysis.

3.3. SSE and Inter-SSE Displacements in GPS Time Series

The detrended time series described above contain some remaining inter-SSE velocities plus transient signals. These need to be separated in order to model motion caused by SSEs. The inter-SSE motions presumably reflect locked periods on the plate interface. We selected periods with both north and east velocities above their 40th percentile values to estimate the remaining inter-SSE velocity at each station (second panel in Figure 6). This is based on the previous study showing that SSEs here occur every ~21 months and can last up to 6 months (Jiang et al., 2012), and GPS stations have reverse displacements during SSE periods. Thus, a 40th percentile can mask out SSE periods but also allow enough data for robust inter-SSE velocity estimates. Gray shades in Figure 6a show an example of the selected inter-SSE periods. For most stations, only periods longer than 6 months are used. Several inland stations do not exhibit significant inter-SSE to SSE transitions due to their long distances from the SSE areas. To ensure sufficient data to estimate inter-SSE velocities, periods longer than 2.5 months are used. Visual inspection of data and the Gaussian wavelet transform (another

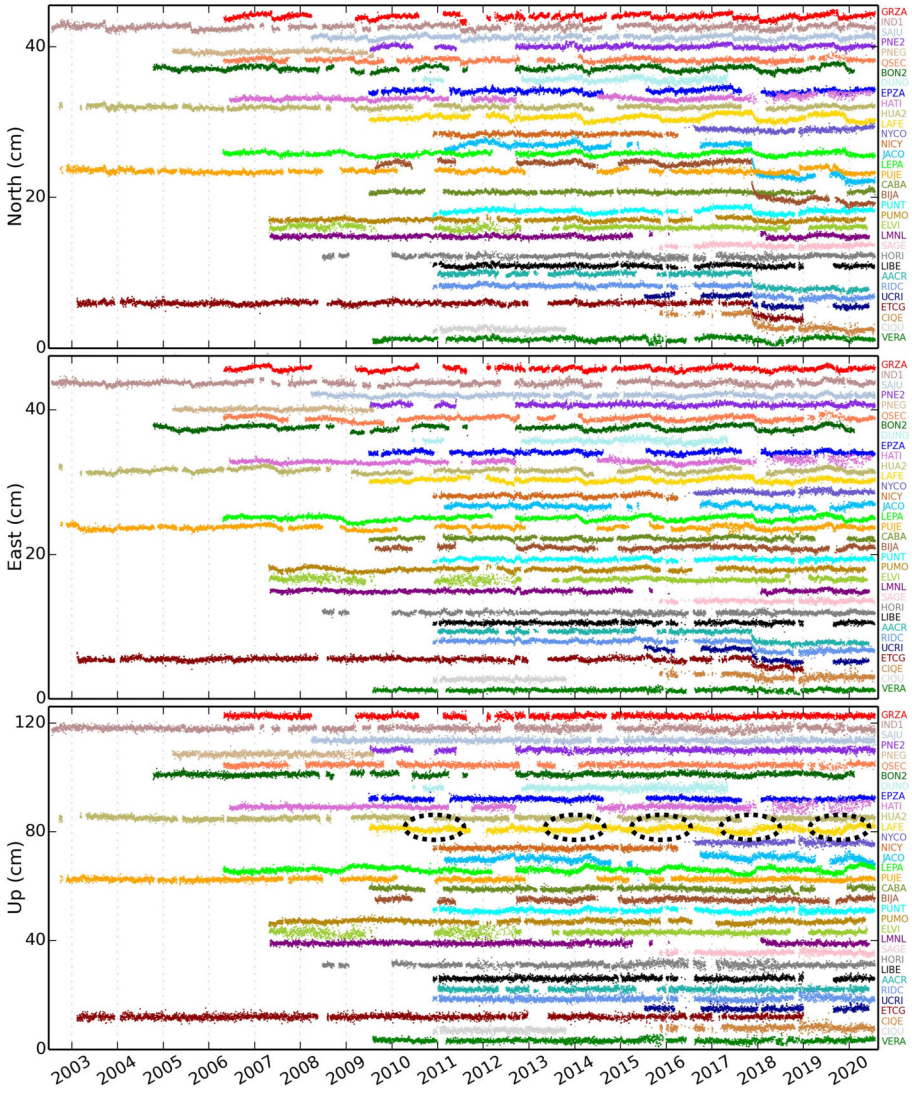

Figure 4. Long-term velocity, 2012 M_w 7.6 earthquake deformation, and annual and semiannual signals removed GPS time series. Displacements are offset for clarity. Dashed ellipses mark examples of several prominent SSE displacements in the vertical component of station LAFE. The three component displacements of station LAFE at expanded scale are presented in the top panel of Figure 6.

way to show SSE to inter-SSE transitions) suggest that this method effectively selects the periods that best represent inter-SSE motion (Figure 6). For each station, the selected periods were fit by a constant slope (remaining inter-SSE velocity) plus multiple Heaviside functions where appropriate (displacements between inter-SSE periods). Figure 7 shows the remodeled position time series with SSEs and the 2017 M_w 6.5 earthquake displacements, plus noise.

4. SSE Slip Inversion

To estimate slow slip on the plate interface, we modeled the GPS-measured SSE displacements in a uniform elastic half-space and solve for time-varying deformation. The curved plate interface (Hayes et al., 2018) in the study area was discretized into 204 planar triangular elements (Figures 8 and 9a) using Gmsh (Geuzaine & Remacle, 2009). The average side length is 26 km, similar to previous studies (e.g., Jiang et al., 2017; Voss et al., 2018). The dislocation model of Meade (2007) was used to calculate Green's functions that relate fault slip to surface displacement. Spatial smoothing was performed using a scale-dependent umbrella operator for neighboring elements (Desbrun et al., 1999; Maerten et al., 2005). We solve a weighted and generalized least squares problem of the form:

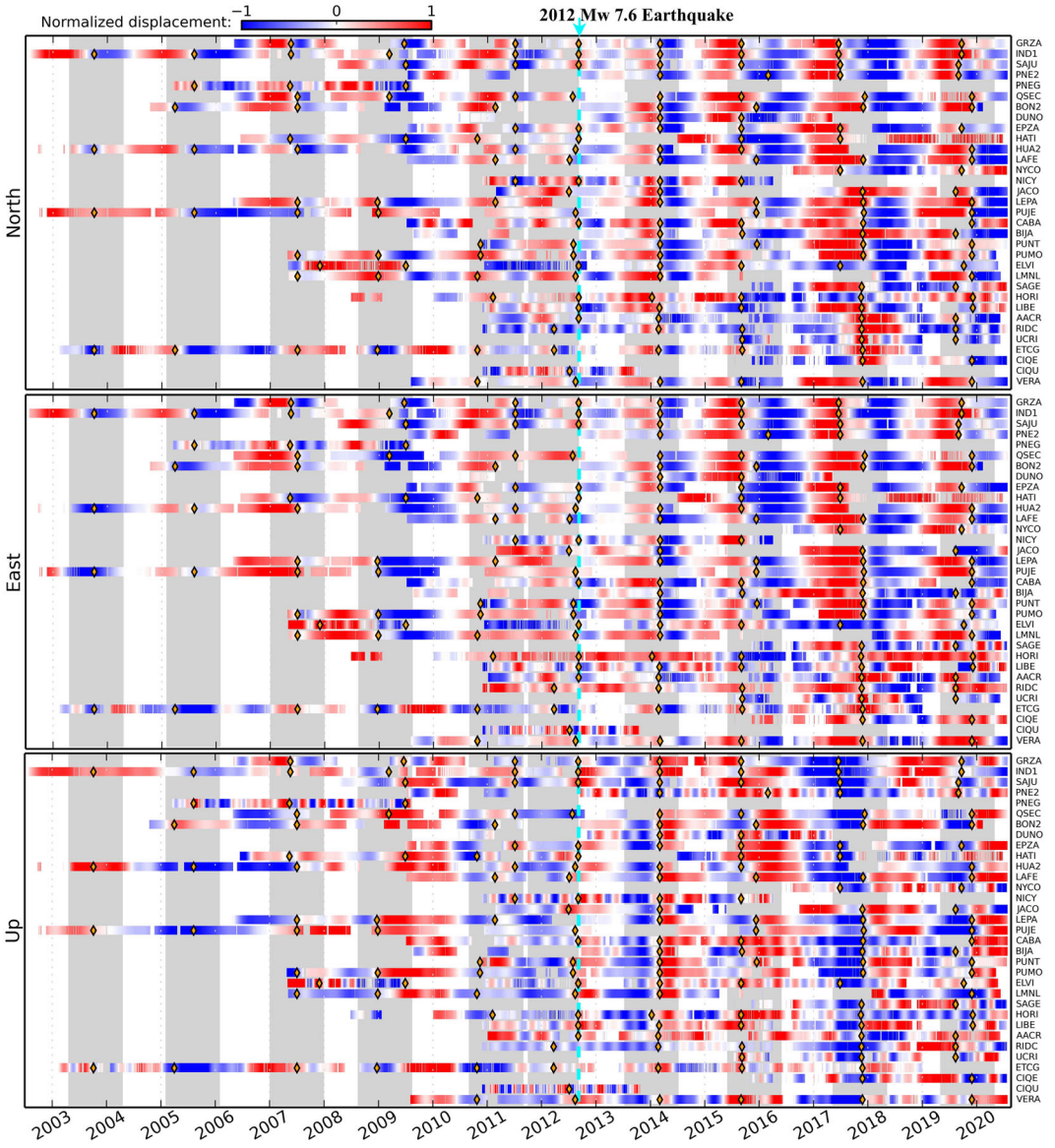

Figure 5. Positionogram of detrended GPS time series. Compared to Figure 4, offset caused by the 2017 M_w 6.5 earthquake is removed. Each row in the positionogram is normalized by the maximum amplitude at the corresponding station. Peak SSE displacements on GPS stations during each modeled period (gray shade) are marked by orange diamonds.

$$\begin{bmatrix} \sqrt{\mathbf{W}}\mathbf{G} \\ \lambda\mathbf{L} \end{bmatrix} \mathbf{m} = \begin{bmatrix} \sqrt{\mathbf{W}}\mathbf{d} \\ \mathbf{0} \end{bmatrix} \tag{2}$$

where **m** is the incremental slip matrix to be solved, **W** is the weight matrix based on GPS precision, **G** is a block lower triangular matrix consisting of the Green's function for each time step, **d** is the data matrix, **L** is a regularization matrix, and λ is the smoothing parameter.

Previous studies (e.g., Jiang et al., 2017) suggest that including a strike-slip component to model SSEs does not improve the data fit. To improve stability and reduce computing load, we did not allow slip in the along-strike direction and imposed a nonnegative constraint in the slip inversion. Except for nonnegativity, no other temporal smoothing was applied. Since a large portion of the modeled area does not have data coverage, to stabilize the inversion, we included a weak zero motion constraint on the edges of the model domain to let slip smoothly taper toward zero.

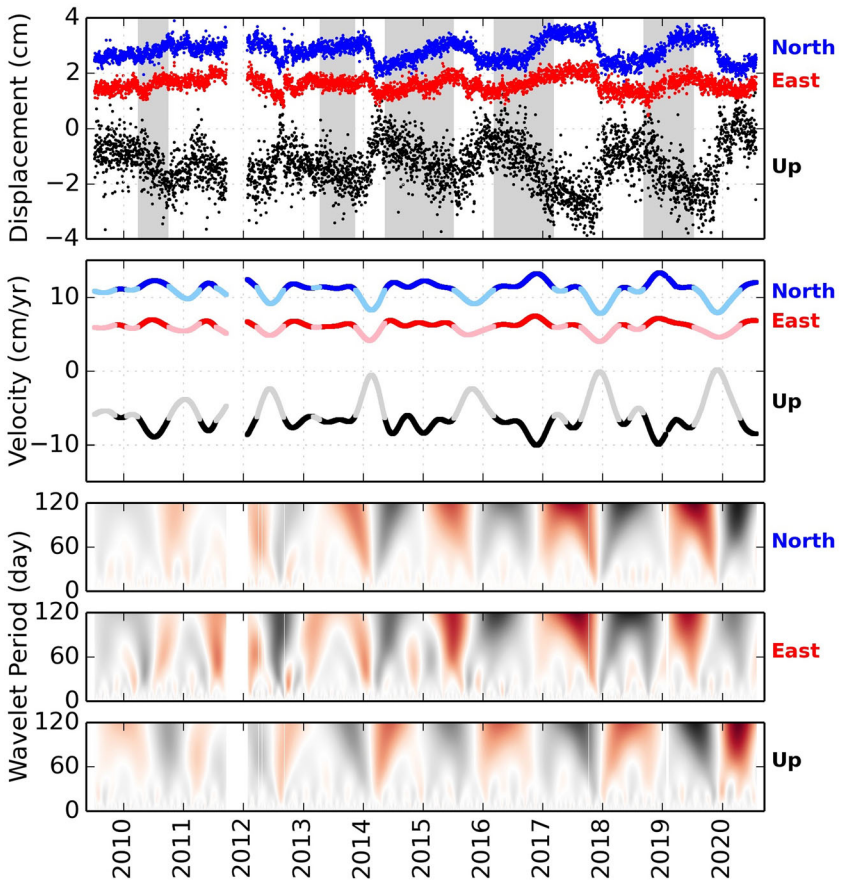

Figure 6. Example of inter-SSE velocity detrending (station LAFE). Top panel shows position time series (offset for clarity). Blue/red/black colors on the second panel mark periods when M-SSA reconstructed speeds of both north and east components are above the 40 percentiles, and periods with duration longer than 180 days are used for inter-SSE velocity estimates (marked by gray bands on the top panel). Bottom three panels show wavelet transform of position times series. Color transitions (red to gray on north and east components, and gray to red on vertical component) correspond to inter-SSE to SSE transitions.

When computing power allows, time-varying fault slip during the entire study period (2002–2020) can be solved in one inversion. Here we downsample the daily time series to 5-day increments and model each of the periods with apparent SSEs. Gray shades in Figure 5 mark ten 1-year periods with inter-SSE to SSE transitions. The GPS network was sparse before 2007 and slip on the plate interface is not well constrained by GPS measurements. After 2007, the number of GPS stations increased significantly and several SSEs have been well documented (Dixon et al., 2014; Jiang et al., 2017; Outerbridge et al., 2010; Voss et al., 2017, 2018). Figures 9a–9h shows cumulative slip on the plate interface within each of the modeled periods (represented by the year of the average date of the modeled maximum speed time for each GPS station during the corresponding period). Table 1 lists the statistics of all major SSEs; the durations are not included because of data noise and our inversion scheme, such that onset and end time for the events are poorly defined due to smoothing. Figure 9j shows cumulative slip for four major SSEs before the 2012 earthquake. Figure 9k shows cumulative slip for three major SSEs after the 2012 earthquake. Supporting information Movies S1–S8 show the time-varying slip and modeled GPS displacements. Figure 10 shows the corresponding moment release rates as a function of time, separated by deep and shallow portions of the plate interface.

We also looked at small SSE-like displacements at a few stations during the inter-SSE periods. These may represent noise, though we cannot preclude the possibility that there are numerous small SSEs missed in our analytical approach. The average slip for all of these for the period 2007–2019 is shown in Figure 9i. We consider the average moment release in this figure (1.1×10^{19} N m, equal to a moment magnitude 6.6 earthquake) to represent our detection threshold for SSEs.

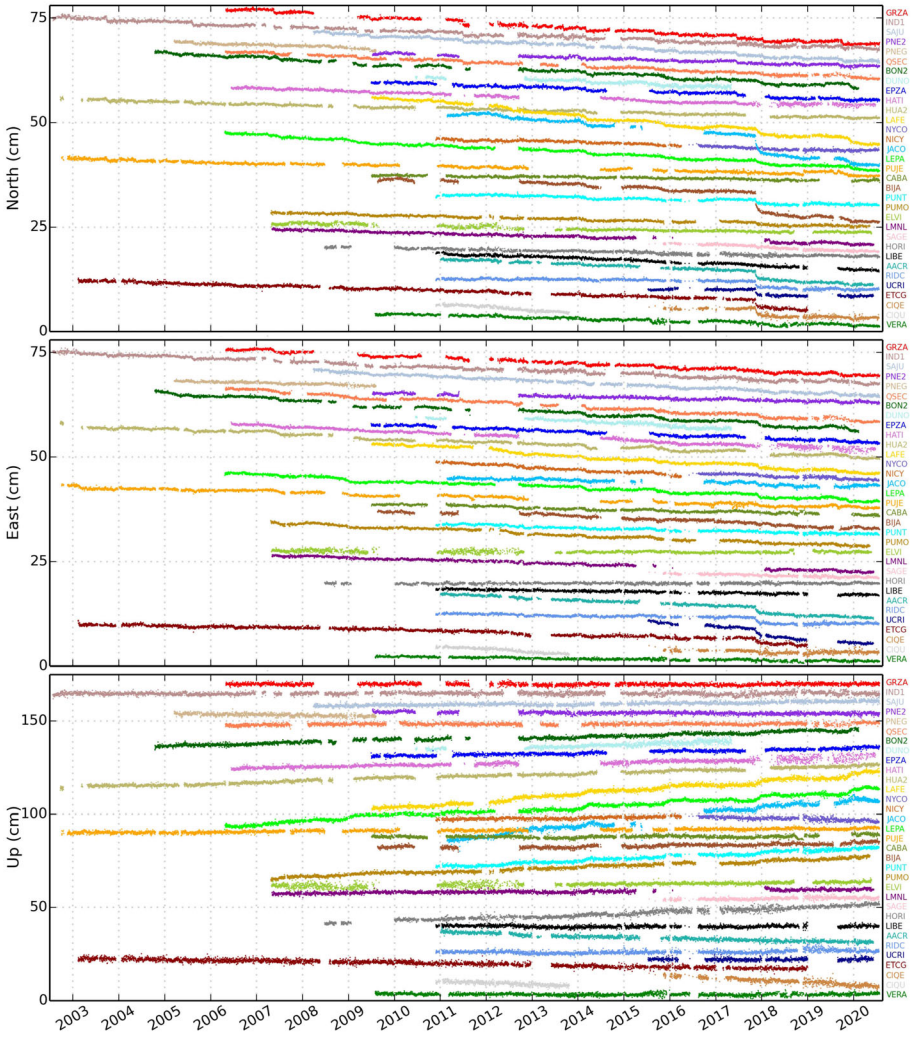

Figure 7. GPS time series with inter-SSE velocity, seasonal oscillations, and 2012 M_w 7.6 earthquake signals removed.

The vertical red line in Figure 9l marks the smoothing parameter that was chosen to maximize smoothing while minimizing residuals. Resolution tests (Figure 8) suggest that fault slip in and close to the Nicoya Peninsula (outlined by orange contour in Figure 8) can be resolved relatively well, while slip far from the Peninsula is not well constrained with existing observations.

While the SSEs exhibit some variability, several common themes emerge: (1) The largest slip is always relatively deep, occurring beneath the entrance of the Nicoya Gulf at ~35 km depth; (2) this deep slow slip generally lasts longer than shallow slow slip; (3) shallow slow slip is more variable in both space and time compared to deep slow slip and also releases less moment; (4) low to zero slow slip occurs where large coseismic displacements occurred in the 2012 M_w 7.6 earthquake; (5) it is difficult to see a consistent pattern of slow slip migration in the time-varying inversions. More detail is given in section 6 below.

5. Inversion for Inter-SSE Locking Rate

Figure 11 shows displacements for the various SSEs at each of the GPS sites as well as the inter-SSE velocity field, the latter presumably showing the effects of locking on the plate interface. Previous studies with data collected before and shortly after the 2012 M_w 7.6 earthquake found that the seismic rupture area closely corresponded with a locked patch identified during the late stage of the seismic cycle using a spatially dense surface velocity field that combined continuous and episodic GPS observations (Feng et al., 2012; Protti

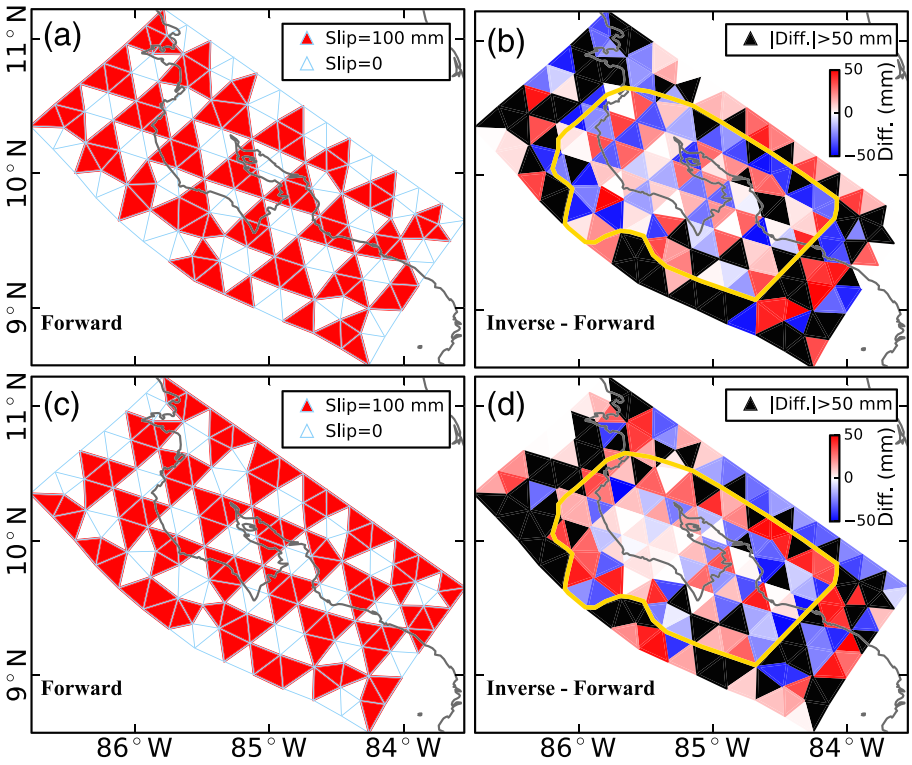

Figure 8. Checkerboard test for the SSE inversion. Left column shows input slip (forward model), note that (c) is the reverse of (a). Right column shows the difference between forward and inverse models. Orange contour outlines the area with slow slip patches where ~100 mm slip can be resolved relatively well with the GPS network.

et al., 2014). Here we use cGPS-measured inter-SSE velocities (thick arrows in Figure 11) to invert for inter-SSE locking on the plate interface. Following the same approach as SSE modeling but in a static inversion scheme, we apply a nonnegativity constraint along the rake direction calculated by the MORVEL plate motion model (DeMets et al., 2010). We find a similar locking pattern before the earthquake but including some areas of frequent slow slip (Figure 12b). For comparison, we also estimated the inter-SSE locking status after the earthquake, that is, the early stage of the earthquake cycle (Figure 12c). Despite the shorter time span and correspondingly higher velocity uncertainties, the inverted locking pattern is similar to the result from the late earthquake cycle stage. Note that for inter-SSE GPS velocity estimates, only stations with more than 1-year data during the identified inter-SSE periods before or after the 2012 M_w 7.6 earthquake are used for these estimates (e.g., red dots in Figure 12a). For the inter-SSE velocity estimates after the 2012 M_w 7.6 earthquake, only data with >200 days after the 2017 M_w 6.5 earthquake (>2,000 days after the 2012 M_w 7.6 earthquake, longer than the longest postseismic relaxation time) are used to minimize the influence of postseismic processes. This limits the total amount of velocity data available to constrain the inversion; hence, the uncertainties in the postearthquake result are somewhat higher than the pre-earthquake result. Figure 12 compares the locking pattern before (b, d) and after (c, e) the earthquake and also compares results with a lower degree of smoothing (b, c) versus a high degree of smoothing (d, e). The similarity between pre-earthquake and post-earthquake locking patterns regardless of smoothing is clear, as is the close correspondence of locking and the 2012 rupture area. However, some locking offshore, south of the peninsula and outside the 2012 rupture area, is also observed regardless of smoothing. We believe this is an important result for future hazard assessments, as discussed below.

6. Discussion

Motion of the Nicoya block not only reflects strain accumulation and release processes on the megathrust but long-term displacement of the block to the northwest at a rate of ~8–10 mm/year. The volcanic arc

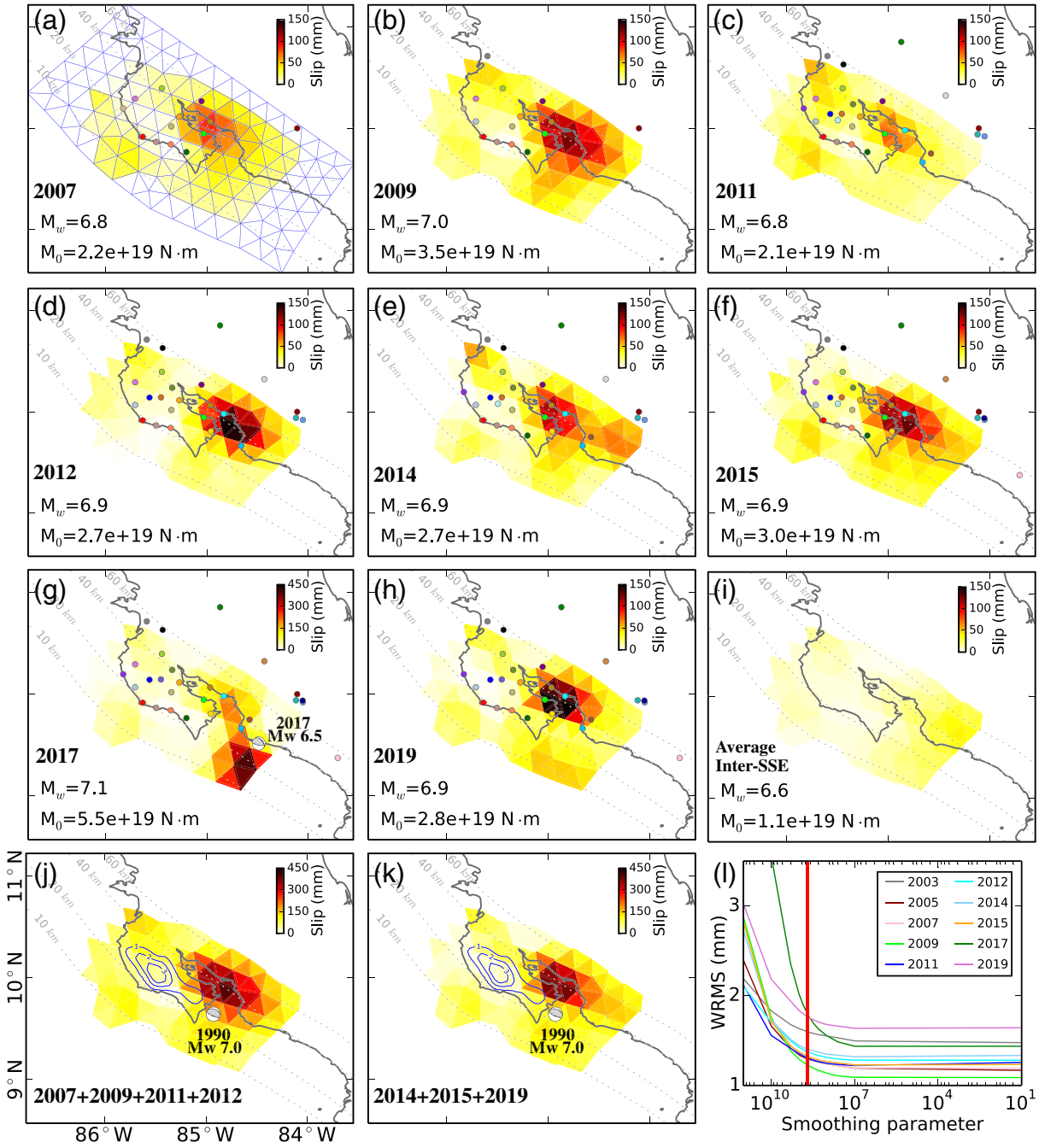

Figure 9. Slip estimate on the plate interface for each selected period. Blue triangular mesh in panel (a) shows the elements that describe the plate interface. Well-resolved model domain is shown, as defined in Figure 8. Colored circles in panels (a)–(h) are GPS stations with data during the modeled period and correspond to the color scheme used in Figure 2. Year label corresponds to the middle time of each period. Moment magnitude (M_w) is calculated using the empirical model of Kanamori (1983). Panel (i) shows the averaged accumulated slip by modeling the six inter-SSE periods (Figure 5) after 2007. Blue contours in panels (j) and (k) show 1, 2, and 3 m coseismic slip for the 2012 M_w 7.6 earthquake (Kyriakopoulos & Newman, 2016). Location and focal mechanism for the 1990 M_w 7.0 earthquake (panels j and k) are from Protti et al. (1995). Note that color scale in (j) and (k) is different from (a) to (i). Panel (l) shows the L-curves; vertical red line marks the preferred smoothing parameter.

marks the boundary between the translating block and the stable Caribbean plate. Northwest motion of the block is accommodated by trench-parallel strike slip faults within the arc, trench-perpendicular bookshelf faults within or near the arc, and diffuse deformation within the arc, driven by some combination of oblique convergence between the Cocos and Caribbean plates and collision of the Cocos Ridge "indentor"

Table 1
Statistics of Modeled SSEs

Named SSEs	Modeled period	Average date of GPS maximum speed[a]	Date of maximum moment rate[b]	Maximum moment rate ($\times 10^{17}$ N m d^{-1})[b]	Total moment release ($\times 10^{19}$ N m)	Equivalent moment magnitude
2003	2003/04/20–2004/04/20	2003/10/05	-	-	-	-
2005	2005/02/01–2006/02/01	2005/06/25	-	-	-	-
2007	2007/01/01–2008/01/01	2007/06/29	2007/07/03	2.8	2.2	6.8
2009	2008/08/15–2009/08/15	2009/03/23	2008/12/21	2.9	3.5	7.0
2011	2010/09/01–2011/09/01	2011/03/07	2010/10/24	1.4	2.1	6.8
2012	2011/10/01–2012/09/05	2012/08/03	2012/08/29	2.0	2.7	6.9
2014	2013/07/10–2014/07/10	2014/03/01	2014/03/05	4.0	2.7	6.9
2015	2015/06/01–2016/06/01	2015/10/01	2015/09/07	2.7	3.0	6.9
2017[c]	2017/05/10–2018/05/10	2017/10/10	2017/11/24	6.7	5.5	7.1
2019	2019/05/01–2020/05/01	2019/10/17	2019/11/30	2.2	2.8	6.9

[a]Calculated by the mean date of the modeled maximum speed time for each recording GPS station in the corresponding study period, marked by diamond symbols in Figure 5. [b]Based on a 30-day average smoothing. [c]Affected by the M_w 6.5 earthquake occurred on 12 November 2017.

(e.g., Ellis et al., 2019; Hobbs et al., 2019; LaFemina et al., 2002; LaFemina et al., 2009; Norabuena et al., 2004). The northwest component of motion is reflected in the different vector azimuths of slow slip displacements (southwest, toward the trench) and inter-SSE velocities (north-northeast in a stable Caribbean plate reference frame) both before and after the earthquake (Figure 11). In other words, SSE displacements are not simply reversed 180° from the direction of inter-SSE strain accumulation, since the inter-SSE motion includes a component of long-term northwest motion of the fore-arc "sliver" block.

Despite the overall similarity of pre-earthquake and postearthquake inter-SSE site velocities, there is a subtle difference in their azimuths that may reflect different rates of northwest block translation. Most of the post-earthquake velocities are rotated slightly counter-clockwise (more northerly) compared to pre-earthquake velocities. This difference in velocity azimuth might indicate a higher rate of northwest block translation after the earthquake by a few mm/year and may reflect reduced resistance to motion, for example, from reduced friction and normal stress on the block's northeast boundary due to trenchward motion of the block associated with coseismic and postseismic motion.

A striking feature of our results is the strong similarity between SSEs before and after the 2012 M_w 7.6 earthquake in terms of moment, slip distribution, and recurrence interval (Figure 9). Similarly, the locking (slip

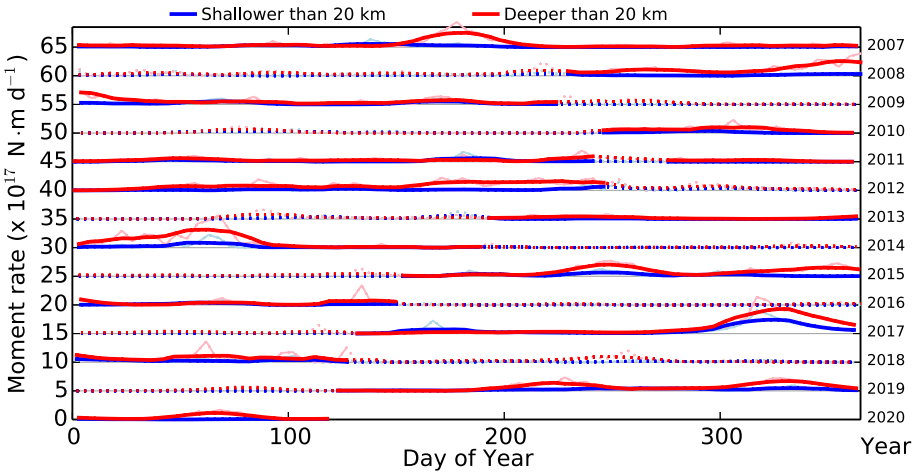

Figure 10. Shallow (blue) and deep (red) SSE moment release rate, smoothed by a 30-day average. Solid and dotted lines correspond to moment release rates for SSE and inter-SSE periods, respectively. For comparison, light blue and pink show a 5-day solution for the shallow and deep portion moment rates, correspondingly. Data are arranged by years (y axis on the right) and are offset for clarity.

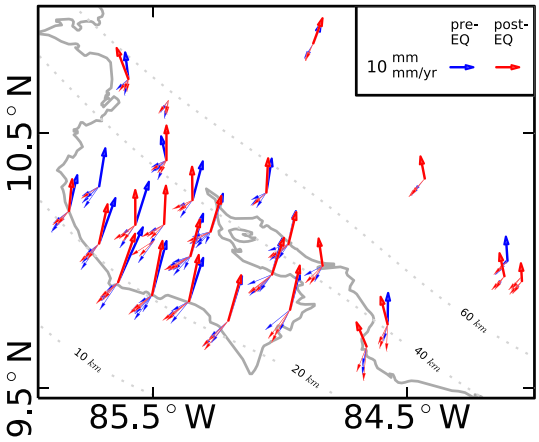

Figure 11. GPS-measured SSE displacements (thin arrows to the southwest) and inter-SSE velocities (thick arrows to the north or north-northeast). Blue and red correspond to periods before and after the 2012 M_w 7.6 earthquake, respectively. Note for inter-SSE velocities, only stations with more than 1-year inter-SSE data (e.g., red dots in Figure 12a) are shown.

deficit) patterns on the plate interface before and after the earthquake are comparable (Figure 12). Below we discuss some implications of these similar pre-earthquake and postearthquake patterns and also address limitations in our SSE catalogue.

6.1. SSE Slip Distribution

Except for the 2017 SSE that coincided with a M_w 6.5 earthquake, a persistent peak slow slip area centered near the entrance of the Nicoya Gulf is evident for all of the modeled periods (Figure 8). While there are several other slow slip areas in some of the modeled periods, notably one near the 10 km deep plate interface offshore the middle of the peninsula, all modeling results suggest minimum or no slow slip over the 2012 M_w 7.6 earthquake rupture area as defined by Yue et al. (2013) or Kyriakopoulos and Newman (2016). This reinforces conclusions of an earlier study that a portion of accumulated strain in some locked areas is released by SSEs and, hence, is less likely participate in the subsequent earthquake (Dixon et al., 2014).

Previous time-dependent modeling suggests that slow slip beneath the Nicoya Peninsula may migrate in a complicated pattern between the shallow and deep portion (e.g., Jiang et al., 2017; Voss et al., 2018). Our modeling results show similar pattern for two well-studied SSEs, including the 2007 SSE (Jiang et al., 2017) and the 2012 SSE (Voss et al., 2018) (Movies S1 and S4). Figure 13 shows the slip distribution pattern at different stages of the 2015 SSE, which is fairly typical. While we do not see a consistent slip migration pattern during the different SSE periods, slow slip in the shallow portion of the plate interface generally lasts for a shorter time than deep slow slip (Movies S1–S8). This can be seen directly in the GPS time series: Figure 13d shows an example of the GPS time series during the 2015 SSE. Two distinct SSE displacements appear on the shallowest stations (e.g., GRZA), both lasting significantly less time than the SSE displacements at stations around the Nicoya Gulf (e.g., LAFE). This is consistent with previously recognized characteristics for deep and shallow SSEs in other places (e.g., Saffer & Wallace, 2015). The periods selected for our time-dependent inversion do not separate shallow and deep SSE displacements in GPS time series but rather were selected based on clustering of SSE displacements in the GPS positionograms (Figure 5). These are dominated by the higher moment deep slip patch (Figure 10); hence, it is possible that we missed some periods of smaller shallow slip. Figure 14a shows the total moment rate of energy release in the study area. Peaks in this figure correspond to maximum slip rates on the deep patch.

6.2. SSE Recurrence

With fewer data and a smaller number of SSEs, previous studies suggested that the deep SSEs in Nicoya Peninsula exhibit predictable behavior while the shallow SSEs are more variable (Voss et al., 2017). With our longer time series, we can estimate the recurrence interval of major SSEs and assess other characteristics with more confidence. The major SSEs are primarily defined by the timing of deep slow slip, since they displace a larger number of GPS stations (Figure 5). We used the modeled maximum speed to represent the onset time of SSE displacement for each station in each study period, marked by diamond symbols in Figure 5, and the mean time in each period to define the middle time of each SSE. While slip distribution is not well constrained before 2007 due to the limited number of GPS stations, the 2003 and 2005 SSEs displaced some GPS stations located above both the shallow and deep portions of the plate interface (Figures 5 and 7). We therefore included these events in the SSE catalogue. Figure 14b shows the recurrence of all major SSEs, roughly corresponding to the peak moment release rate shown in Figure 14a. The average recurrence interval is 21.7 $\pm$ 2.6 months (one standard derivation), similar to the previous estimate of 21 $\pm$ 6 months by Jiang et al. (2012) using data obtained before 2012.

The Kolmogorov-Smirnov (K-S) test was used by Voss et al. (2017) to determine if the 2012 M_w 7.6 earthquake changed the SSE recurrence interval. They found that SSE recurrence is steady across the earthquake, that is, the recurrence interval of large SSEs was not affected by this event, a surprising result. Here we use the same approach to test the predictability of SSEs, by comparing the observed distribution with a constant

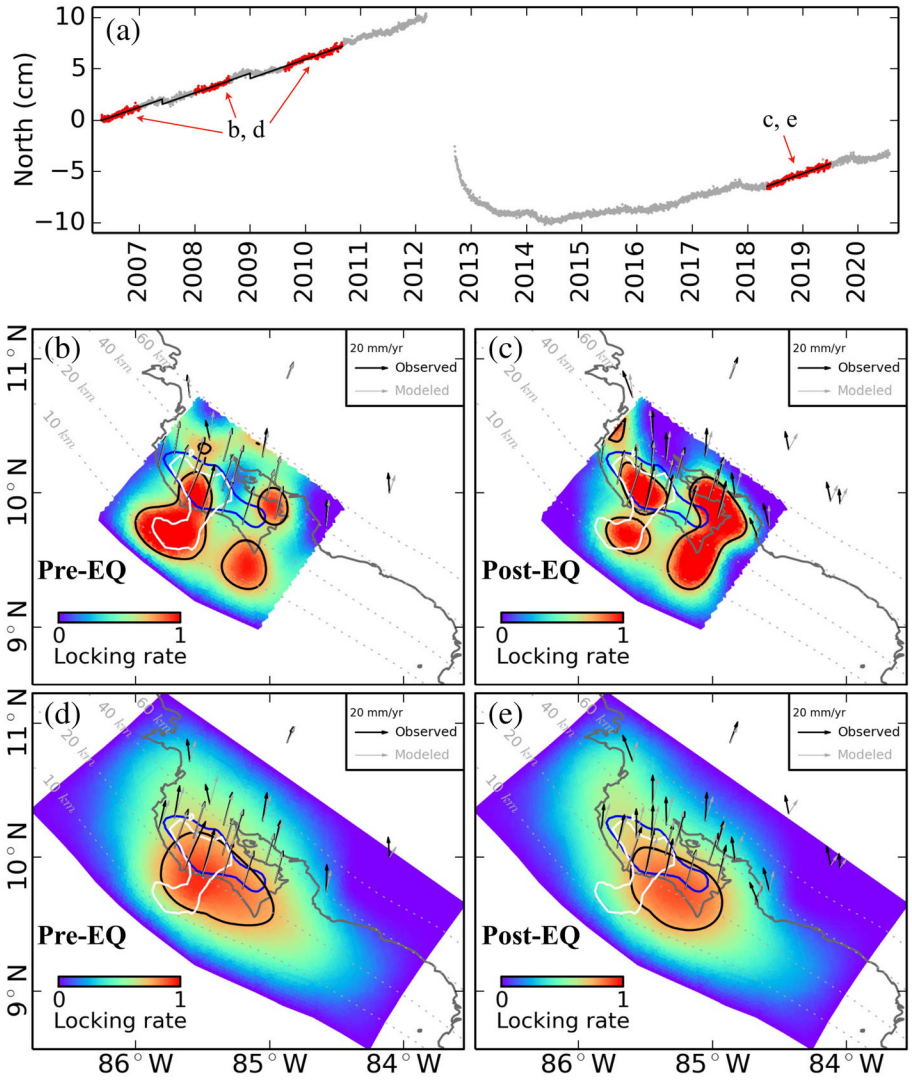

Figure 12. Inter-SSE locking status before and after the 2012 M_w 7.6 earthquake. (a) North component GPS displacement (seasonal oscillations removed) of station LEPA. Red dots are used to estimate inter-SSE velocities before and after the 2012 M_w 7.6 earthquake. (b, d) Inter-SSE locking rate before the 2012 M_w 7.6 earthquake. (c, e) Inter-SSE locking rate after the 2012 M_w 7.6 earthquake. Here locking rate 0 represents fault slipping at the plate rate, 1 represents fully locked. Black contours outlines areas where locking rate is >0.75. Blue and white contours show the >1 m seismic rupture area from Kyriakopoulos and Newman (2016) and Yue et al. (2013), respectively. (b and c) Locking estimates using a smoothing factor picked by L-curve, areas far from the GPS network are masked out. (d and e) Highly smoothed results.

recurrence rate (Zwillinger & Kokoska, 1999). Figure 14c illustrates the K-S test for the identified SSEs. Based on the critical value, the observed recurrence can be described by a constant recurrence rate distribution. We note that the calculated recurrence interval is based on SSEs that are dominated by the deep events and, hence, may not be useful for predicting shallow slow slip, which appears to be more frequent but more irregular, both spatially and temporally.

Based on different shallow slow slip behavior and a change in moment release between the 2014 and 2015 SSEs, Voss et al. (2017) concluded that strain released by these two events is not constant despite the similarity in recurrence rate. While we do observe a lower moment release in the 2014 SSE compared to the 2015 SSE, we also find that shallow slow slip is present in 2014 (Figure 9e and supporting information Movie S5), and we do not see a significant change in total strain release for the different SSEs (Table 1). The average moment release for SSEs before the 2012 M_w 7.6 earthquake (2007, 2009, 2011, and 2012) is

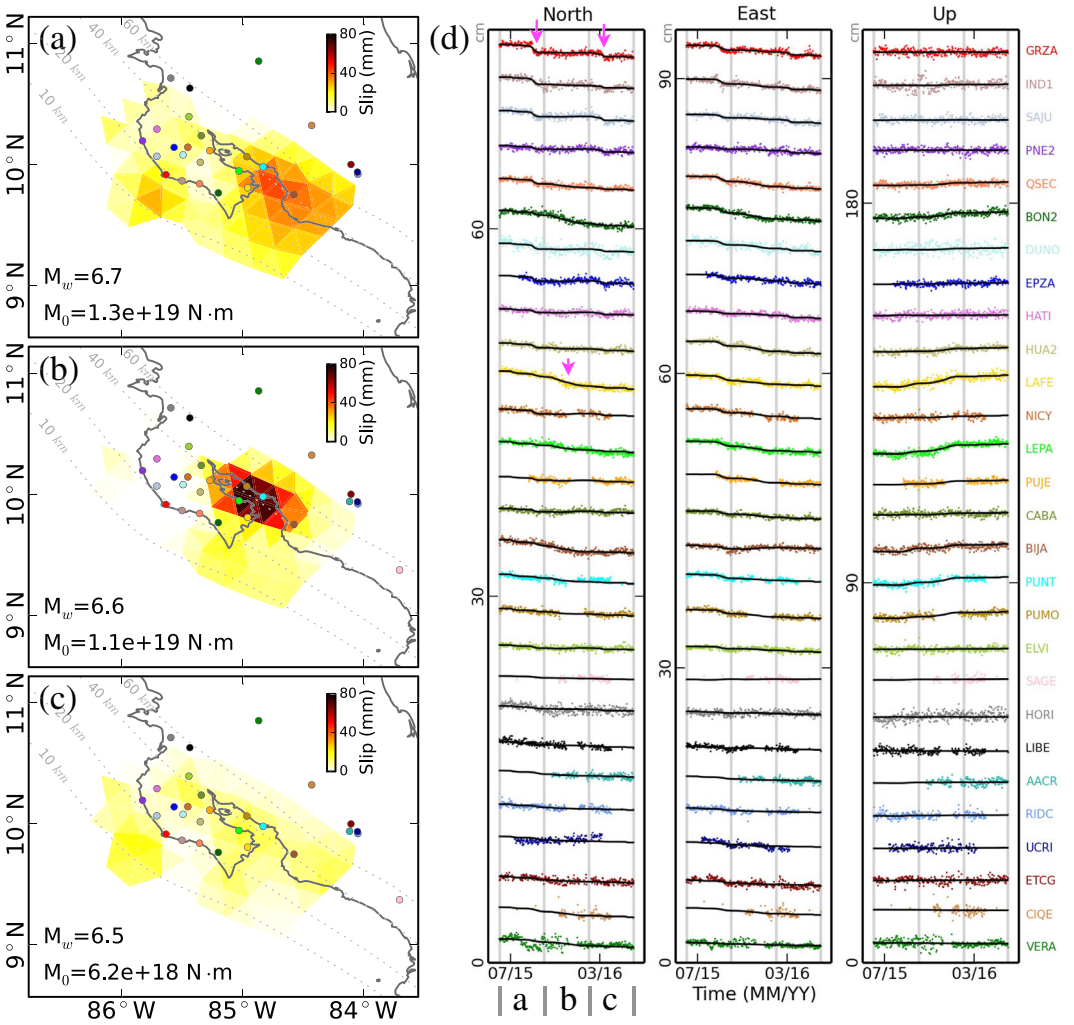

Figure 13. Cumulative slip in three 4-month periods during the 2015 SSE. Colored circles in (a)–(c) correspond to GPS stations; their time series (dots) and modeled predicted displacements (black lines) are shown in (d), offset for clarity. Vertical gray lines in (d) mark three periods (4 months each) with their cumulative inverted slip shown in (a)–(c). Note the shallow and deep SSE duration difference reflected in some GPS displacement time series (marked by magenta arrows).

$2.6 \pm 0.6 \times 10^{19}$ N m (~M_w 6.9), while it is $2.8 \pm 0.1 \times 10^{19}$ N m (~M_w 6.9) after the 2012 M_w 7.6 earthquake (2014, 2015, and 2019). The higher moment release for the 2015 SSE found by Voss et al. (2017) is not observed on our data set, and probably reflects weaker data constraints in the earlier study—we have additional data in the southeast part of the network that were not available to Voss et al. (2017).

6.3. Inter-SSE Locking

Reid's elastic strain hypothesis for earthquakes holds that regions of the brittle upper crust that are locked and accumulating elastic strain as a result of relative plate or block motion will eventually experience an earthquake, releasing accumulated strain (Reid, 1910). One of the satisfying results of the multidecade geodetic monitoring effort in northwestern Costa Rica was a clear confirmation of this simple hypothesis. Analysis of data collected before and just after the 2012 earthquake showed a strong correlation between the interseismic or inter-SSE locking pattern and the subsequent area of seismic rupture (Dixon et al., 2014; Feng et al., 2012; Kyriakopoulos & Newman, 2016; Protti et al., 2014; Yue et al., 2013). It is of great interest whether such behavior is stationary, that is, does the pre-earthquake pattern of strain accumulation, indicating which parts of the plate interface are locked, change as a result of the earthquake?

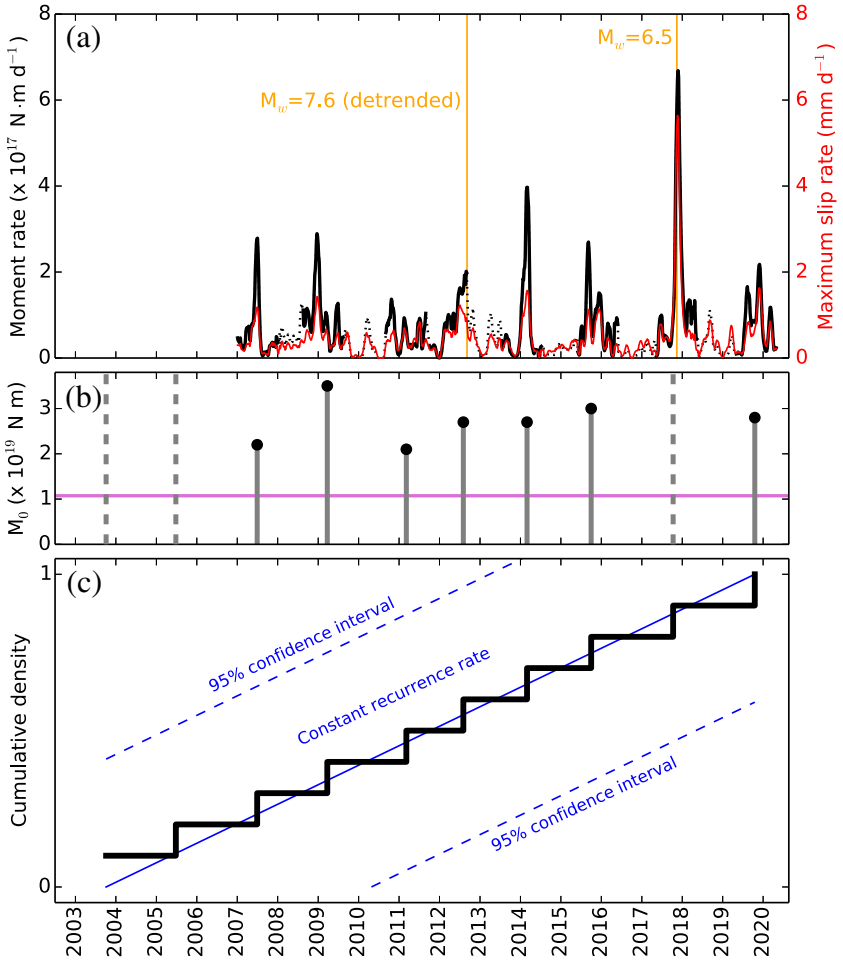

Figure 14. SSE statistics. (a) Moment release rate and maximum slow slip rate since 2007, smoothed by a 30-day average. Solid and dotted black lines correspond to moment rate for SSE and inter-SSE periods, respectively. Red line shows maximum slip rate on the plate interface. (b) SSE recurrences and moment release during the study period. SSEs before 2007 are not well constrained, and the SSE in 2017 was affected by the M_w 6.5 earthquake (dashed line). Purple line marks the SSE detection threshold (M_w 6.6). (c) Kolmogorov-Smirnov (K-S) test statistics of SSE recurrence. Black line shows sample distribution function. Solid blue line shows a theoretical constant recurrence rate; dashed blues mark the 95% confidence interval for the critical value (0.409) of one sample K-S test with 10 observations (Zwillinger & Kokoska, 1999). The maximum absolute difference (0.1) between the sample and the constant recurrence distribution is smaller than the critical value, indicating that the SSE recurrence can be described by a continuous distribution function.

Figure 12 compares the inter-SSE locking rate for the late and early stages of the earthquake cycle. Due to limited data coverage and short postseismic span, the postearthquake inversion is less well constrained, and we include highly smoothed inversion results for comparison (Figures 12d and 12e). With this limitation, the pre-earthquake and postearthquake data show essentially the same highly coupled zone beneath parts of the Nicoya Peninsula, clearly overlapping the rupture area of the 2012 M_w 7.6 earthquake (Figure 12).

One locked area that did not participate in the 2012 earthquake shows up in both the pre-earthquake and postearthquake strain accumulations estimates (Figures 12b and 12c) and coincides with the deep SSE slip patch (Figure 9). The high rate of moment release that we estimate for the SSEs here appears to be sufficient to release all or most accumulated interseismic strain. In contrast, both pre-earthquake and postearthquake strain accumulation estimates imply significant strain accumulation offshore that was *not* released in the 2012 earthquake (Figure 12). Figure 10 also shows significantly less strain release in shallow SSEs compared to deep SSEs. While the postearthquake strain accumulation estimate suffers from limited data, the pre-earthquake estimate is relatively well constrained. This implies that the 2012 earthquake released

only a fraction of accumulated offshore strain, with the remainder to be released in a future event. The implication is that strain can be stored over more than one seismic cycle (e.g., Salditch et al., 2020) and the magnitude of the last few earthquakes in a repeating pattern is not necessarily representative of the maximum magnitude of future earthquakes (e.g., McCaffrey, 2007). The offshore strain accumulation patch suggested by our limited data is an obvious candidate for future offshore geodetic observations.

6.4. Effect of Stress Changes From the 2012 M_w 7.6 Earthquake

Previous studies have suggested that slow slip can be sensitive to stress changes, including the presumably large changes caused by earthquakes and possibly including stress changes as small as tidal variations (e.g., Hawthorne & Rubin, 2010; Wallace et al., 2018). While the 2012 M_w 7.6 earthquake caused large and long-lasting stress perturbations on the Central American megathrust, a surprising result of our study is that the location, recurrence interval, and magnitude of major SSEs in northwestern Costa Rica remained essentially unchanged by the earthquake, using data for an 18-year period that span the late to early stages of an earthquake cycle. The earthquake cycle here is approximately 50–60 years in duration (e.g., Protti et al., 2014); hence, our observation period constitutes 30–40% of this cycle. Similarly, the locking pattern appears to be similar pre-earthquake and post-earthquake. This regularity of both major SSEs and locking patterns across the 2012 M_w 7.6 earthquake time boundary suggests that frictional conditions on this particular megathrust are insensitive to stress perturbations. One interpretation is that the patterns of both slow slip and strain accumulation are driven by long-lived geologic conditions that are largely unaffected by earthquake cycle stress perturbations. For example, the deep slow slip patch may reflect a long-lived asperity associated with subduction of a seamount that was part of the Fisher Seamount Chain (Figure 1). The deep slow slip patch is directly on strike with the exposed part of the chain on the Cocos plate, as well as a "scar" in the forearc bathymetry just inboard of where the chain first enters the trench. A patch interpreted as a decapitated seamount between this "scar" and our deep SSE patch (beach ball in Figures 9j and 9k) ruptures with M_w 7.0 $\pm$ 0.1 earthquakes every ~50 years (1882, 1939, and 1990) (Protti et al., 1995).

6.5. Limitations of our SSE Catalogue

The SSE catalogue generated by this study consists of relatively large SSEs ($M_w > 6.6$) that occurred from 2002 to 2020 and displaced a large number of GPS stations across the network. There are limitations in the catalogue, primarily due to limited data coverage. These include (1) sparse site distribution before 2007, (2) data gaps due to maintenance difficulties, and (3) geometric limitations, since there are no seafloor geodetic sites. These are discussed below.

The continuous GPS network initiated in 2002 with only three stations. The number of total stations increased slowly in the first 5 years but had nearly tripled by 2007. The total number of GPS stations in the network approached the present level by the end of 2010, well before the 2012 M_w 7.6 earthquake (Dixon et al., 2013), allowing better documentation of later SSEs and good coverage of the 2012 earthquake and associated postseismic processes (Figure 2). Previous studies of SSEs in Nicoya Peninsula mainly focused on events in or after 2007 (Dixon et al., 2014; Jiang et al., 2017; Outerbridge et al., 2010; Voss et al., 2017, 2018). GPS-measured displacements centering on 2003 and 2005 clearly reveal SSE occurrence, though details of slip distribution on the plate interface cannot be discerned.

Data gaps may also limit SSE identification. Figure 15a shows an example at station GRZA. There is a ~1-year data gap in 2008–2009. Comparison of time series before and after this gap suggests one or more SSEs may have occurred during the data gap. Elevated seismic tremor in August 2008 is consistent with this hypothesis (Outerbridge et al., 2010; Walter et al., 2011).

Limited geodetic coverage reduces our ability to detect smaller SSEs, especially offshore. Previous studies discussed resolution limitations in displacement monitoring, either using a checkerboard test (e.g., Dixon et al., 2014; Jiang et al., 2017; Kyriakopoulos & Newman, 2016; Protti et al., 2014; Voss et al., 2017) or with a model resolution matrix (Kyriakopoulos & Newman, 2016; Outerbridge et al., 2010). In general, slip resolution decreases toward the trench, and the current cGPS network is unable to resolve small SSEs there (e.g., Dixon et al., 2014). Limited seafloor geodetic measurements show evidence of SSEs occurring within 1 km to the trench (Davis et al., 2011). Combining measurements from seafloor pressure sensors near the trench and terrestrial GPS, Jiang et al. (2017) documented a SSE in 2007 that initiated at the shallow portion of the subduction plate interface (~15 km deep) and propagated all the way to the trench. Such SSEs are

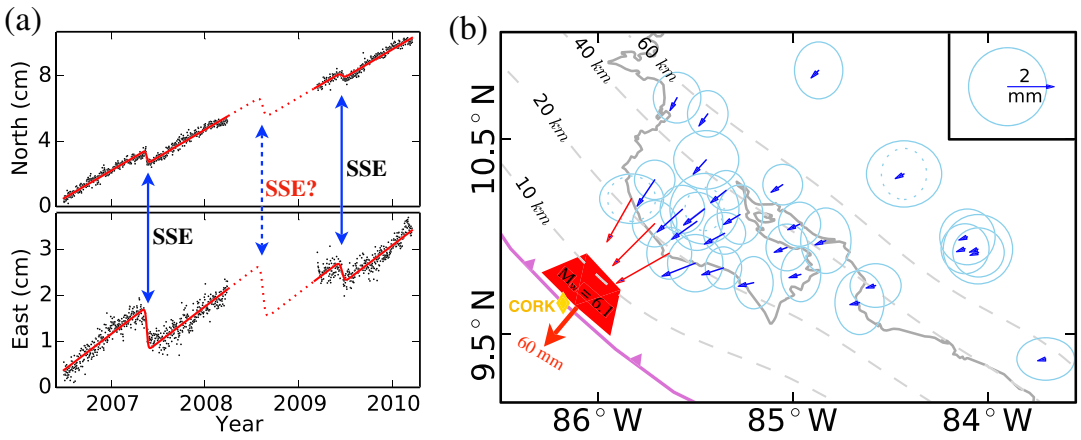

Figure 15. Examples of the limitations of the SSE catalogue. (a) Example of a possible slow slip event that occurred during a data gap at station GRZA. Black dots show horizontal displacements. Red lines are best fitting models with constant secular rate and SSE or possible SSE displacements. Note that Walter et al. (2011) analyzed 4 years of seismic data (2006–2009) collected in the Nicoya Peninsula and found elevated tremor activity in August 2008, as well as in May 2007 and April 2009 (Figures 1 and 3 in Walter et al., 2011). (b) Example of a synthetic SSE with moderate fault slip (60 mm slip, equivalent to M_w 6.1) occurring on the red patch near the trench where Davis et al. (2011) found evidence of slow slip using borehole data (CORK site). Thin arrows show predicted horizontal displacements at the GPS locations. Predicted vertical displacements are all smaller than 0.5 mm and omitted for clarity. Ellipses show average weighted root-mean-square (WRMS) of the residuals for the horizontal components of the modeled SSEs (dashed ellipses are decommissioned sites). Only three stations (red) have predicted horizontal displacements that are significantly larger than corresponding WRMS.

difficult to detect with the current terrestrial GPS network due to low signal-to-noise ratio (Figure 15b). This may explain the relatively more frequent but irregular SSE displacements measured by GPS located above the shallow portion of the subduction zone.

Several large earthquakes occurred near the identified SSEs in this study, including the 2012 M_w 7.6 earthquake and the 2017 M_w 6.5 earthquake. While the 2012 M_w 7.6 earthquake was preceded by a SSE, previous modeling effort suggests that the SSE caused a Coulomb stress change that is significantly smaller than typical thresholds for earthquake triggering (Voss et al., 2018). The 2017 M_w 6.5 earthquake may have occurred before or shortly after the beginning of a SSE (Figures 4–7). However, only a limited number of GPS sites have significant coseismic displacements compared to noise for this event. Data limitation and noise in inversions make it difficult to reliably determine if one triggers another.

Smoothing in the slip inversions increases the uncertainty of onset time for SSEs. We note that for the part of the Central American subduction zone studied here, the long-duration of deep SSEs (several months) and the complicated SSE migration patterns are not consistent with some earthquake triggering models such as power law acceleration in fault slip (e.g., Kato et al., 2016). Better data offshore, improved noise reduction techniques, and improved slip inversion methods are needed for better understanding of slip migration and earthquake triggering.

Despite these limitations in our SSE catalogue, available data strongly suggest that moment release via SSEs on the shallow portion of the seismogenic plate interface is consistently lower than deep portions (Figures 9, 10, 12, and 13, with depth contours of plate interface shown in gray). Since both the shallow and deep portions of the seismogenic plate interface have locked patches (i.e., areas with high locking rate; Figure 12) that are accumulating elastic strain at high rates during inter-SSE periods, and the shallow patches release much lower amounts of strain during earthquakes and SSEs, unreleased strain on these shallow portions of the megathrust must accumulate strain in the long-term (i.e., across multiple seismic cycles) (Salditch et al., 2020). Longer data span and better offshore coverage will help to improve such strain budget estimates and better constrain forecasts of future earthquake magnitude and tsunami potential.

7. Conclusions

We report analyses of continuous GPS data in or near the Nicoya Peninsula of Costa Rica for the period 2002–2020. Ten clusters of SSE displacements were analyzed to form a catalogue, all with moment magnitude greater than 6.6. The recurrence rate of SSEs at or above this level is 21.7 ± 2.6 months. The

SSE recurrence rate, moment release rate, and location of maximum slow slip were unchanged by the 2012 M_w 7.6 earthquake. Time-varying slip inversion suggests that slow slip in and near Nicoya Peninsula distributes around the 2012 seismic rupture area, with peak slip persisting beneath the entrance of the Nicoya Gulf. While SSEs occur at both the shallow and deep portions of the plate interface, deep SSEs release a much larger portion of accumulated strain and are more predictable compared to shallow SSEs. Inter-SSE strain accumulation characteristics also remain unchanged from the late to early stages of the earthquake cycle despite strong stress perturbations from the 2012 earthquake. In particular, the rupture area of the 2012 earthquake, which coincided with a pre-earthquake locked patch, has relocked and continues to accumulate strain at or close to the plate motion rate. Other regions of significant inter-SSE locking include the deep slow slip patch (where accumulated strain is largely released by frequent slow slip) and some offshore patches which did not participate in the 2012 earthquake, did not experience significant afterslip, and do not release significant strain by SSEs. These areas warrant improved monitoring by offshore geodetic techniques, as they appear to have the potential to rupture in seismic events larger than the recent historical record would suggest.

Data Availability Statement

Data collected at DUNO, HORI, and JACO stations are contributed by the Observatorio Vulcanológico y Sismológico de Costa Rica at Universidad Nacional (OVSICORI-UNA) and can be requested from Marino Protti (marino.protti.quesada@una.cr). Data collected at CIQE, CIQU, LIBE, NICY, NYCO, PUNT, RIDC, and SAGE stations can be found from the Instituto Geográfico Nacional website (https://gnss.rnp.go.cr/SBC/). Daily position time series of ETCG, UCRI, and AACR stations were provided by the Nevada Geodetic Laboratory (Blewitt et al., 2018). All the other GPS data used in this paper are archived at the UNAVCO repository, their names and DOI links are as follows: GRZA (https://doi.org/10.7283/T5HX19V3); IND1 (https://doi.org/10.7283/T58C9TDT); SAJU (https://doi.org/10.7283/T5F47M9C); PNE2 (https://doi.org/10.7283/T5D50K43); PNEG (https://doi.org/10.7283/T50V89ZR); QSEC (https://doi.org/10.7283/T5SF2TBM); BON2 (https://doi.org/10.7283/T5W66HXJ); EPZA (https://doi.org/10.7283/T5JW8C1S); HATI (https://doi.org/10.7283/T5X34VM5); HUA2 (https://doi.org/10.7283/T5RF5S67); LAFE (https://doi.org/10.7283/T57D2S80); LEPA (https://doi.org/10.7283/T5NP22M8); PUJE (https://doi.org/10.7283/T54M92PG); CABA (https://doi.org/10.7283/T5GX48QQ); BIJA (https://doi.org/10.7283/T5C53J0Q); PUMO (https://doi.org/10.7283/T55M63V9); ELVI (https://doi.org/10.7283/T59C6VKN); LMNL (https://doi.org/10.7283/T51V5C3J); and VERA (https://doi.org/10.7283/T5MP51FF).

Acknowledgments

This research was supported by National Science Foundation grants 1345100 and 1835947 to T. H. D. We thank Matt Wei for suggesting this study. Seth Stein and an anonymous reviewer are acknowledged for their careful and constructive comments. We thank Editors Paul Tregoning and Mike Poland for their quick and thoughtful feedback. Most of the stations reported here are jointly operated by OVSICORI-UNA and UNAVCO, and we thank personnel at these institutions for network maintenance. We thank JPL for providing the GipsyX software for GPS data processing.

References

Blewitt, G., Hammond, W. C., & Kreemer, C. (2018). Harnessing the GPS data explosion for interdisciplinary science. *Eos*, *99*. https://doi.org/10.1029/2018EO104623

Böhm, J., Werl, B., & Schuh, H. (2006). Troposphere mapping functions for GPS and very long baseline interferometry from European Centre for Medium-Range Weather forecasts operational analysis data. *Journal of Geophysical Research*, *111*, B02406. https://doi.org/10.1029/2005JB003629

Bürgmann, R. (2018). The geophysics, geology and mechanics of slow fault slip. *Earth and Planetary Science Letters*, *495*, 112–134.

Davis, E., Heesemann, M., & Wang, K. (2011). Evidence for episodic aseismic slip across the subduction seismogenic zone off Costa Rica: CORK borehole pressure observations at the subduction prism toe. *Earth and Planetary Science Letters*, *306*(3–4), 299–305.

DeMets, C., Gordon, R. G., & Argus, D. F. (2010). Geologically current plate motions. *Geophysical Journal International*, *181*(1), 1–80.

Desbrun, M., Meyer, M., Schröder, P. & Barr, A.H. (1999). Implicit fairing of irregular meshes using diffusion and curvature flow. In Proceedings of the 26th annual conference on Computer graphics and interactive techniques, 317–324.

Dixon, T. H., Jiang, Y., Malservisi, R., McCaffrey, R., Voss, N., Protti, M., & Gonzalez, V. (2014). Earthquake and tsunami forecasts: Relation of slow slip events to subsequent earthquake rupture. *Proceedings of the National Academy of Sciences*, *111*(48), 17,039–17,044.

Dixon, T. H., Schwartz, S., Protti, M., González, V., Newman, A., Marshall, J., & Spotila, J. (2013). Detailed data available for recent Costa Rica earthquake. *Eos, Transactions American Geophysical Union*, *94*(2), 17–18.

Dong, D., Fang, P., Bock, Y., Cheng, M. K., & Miyazaki, S. I. (2002). Anatomy of apparent seasonal variations from GPS-derived site position time series. *Journal of Geophysical Research*, *107*(B4), 2075. https://doi.org/10.1029/2001JB000573

Douglas, A., Beavan, J., Wallace, L., & Townend, J. (2005). Slow slip on the northern Hikurangi subduction interface, New Zealand. *Geophysical Research Letters*, *32*, L16305. https://doi.org/10.1029/2005GL023607

Dragert, H., Wang, K., & James, T. S. (2001). A silent slip event on the deeper Cascadia subduction interface. *Science*, *292*(5521), 1525–1528. https://doi.org/10.1126/science.1060152

Ellis, A., DeMets, C., McCaffrey, R., Briole, P., Cosenza Muralles, B., Flores, O., et al. (2019). GPS constraints on deformation in northern Central America from 1999 to 2017, Part 2: Block rotations and fault slip rates, fault locking and distributed deformation. *Geophysical Journal International*, *218*(2), 729–754.

Feng, L., Newman, A. V., Protti, M., González, V., Jiang, Y., & Dixon, T. H. (2012). Active deformation near the Nicoya Peninsula, northwestern Costa Rica, between 1996 and 2010: Interseismic megathrust coupling. *Journal of Geophysical Research*, *117*, B06407. https://doi.org/10.1029/2012JB009230

Geuzaine, C., & Remacle, J. F. (2009). Gmsh: A three-dimensional finite element mesh generator with built-in pre- and post-processing facilities. *International Journal for Numerical Methods in Engineering*, *79*(11), 1309–1331.

Hawthorne, J. C., & Rubin, A. M. (2010). Tidal modulation of slow slip in Cascadia. *Journal of Geophysical Research*, *115*, B09406. https://doi.org/10.1029/2010JB007502

Hayes, G. P., Moore, G. L., Portner, D. E., Hearne, M., Flamme, H., Furtney, M., & Smoczyk, G. M. (2018). Slab2, a comprehensive subduction zone geometry model. *Science*, *362*(6410), 58–61. https://doi.org/10.1126/science.aat4723

Hobbs, T. E., Kyriakopoulos, C., Newman, A. V., Protti, M., & Yao, D. (2017). Large and primarily updip afterslip following the 2012 M_w 7.6 Nicoya, Costa Rica, earthquake. *Journal of Geophysical Research: Solid Earth*, *122*, 5712–5728. https://doi.org/10.1002/2017JB014035

Hobbs, T. E., Newman, A. V., & Protti, M. (2019). Enigmatic upper-plate sliver transport paused by megathrust earthquake and afterslip. *Earth and Planetary Science Letters*, *520*, 87–93.

Jiang, Y., Liu, Z., Davis, E. E., Schwartz, S. Y., Dixon, T. H., Voss, N., et al. (2017). Strain release at the trench during shallow slow slip: The example of Nicoya Peninsula, Costa Rica. *Geophysical Research Letters*, *44*, 4846–4854. https://doi.org/10.1002/2017GL072803

Jiang, Y., Wdowinski, S., Dixon, T. H., Hackl, M., Protti, M., & Gonzalez, V. (2012). Slow slip events in Costa Rica detected by continuous GPS observations, 2002-2011. *Geochemistry, Geophysics, Geosystems*, *13*, Q04006. https://doi.org/10.1029/2012GC004058

Kanamori, H. (1983). Magnitude scale and quantification of earthquakes. *Tectonophysics*, *93*(3–4), 185–199.

Kato, A., Fukuda, J. I., Kumazawa, T., & Nakagawa, S. (2016). Accelerated nucleation of the 2014 Iquique, Chile M_w 8.2 earthquake. *Scientific Reports*, *6*, 24792.

Kedar, S., Hajj, G. A., Wilson, B. D., & Heflin, M. B. (2003). The effect of the second order GPS ionospheric correction on receiver positions. *Geophysical Research Letters*, *30*(16), 1829. https://doi.org/10.1029/2003GL017639

Kyriakopoulos, C., & Newman, A. V. (2016). Structural asperity focusing locking and earthquake slip along the Nicoya megathrust, Costa Rica. *Journal of Geophysical Research: Solid Earth*, *121*, 5461–5476. https://doi.org/10.1002/2016JB012886

LaFemina, P., Dixon, T. H., Govers, R., Norabuena, E., Turner, H., Saballos, A., et al. (2009). Fore-arc motion and Cocos Ridge collision in Central America. *Geochemistry, Geophysics, Geosystems*, *10*, Q05S14. https://doi.org/10.1029/2008GC002181

LaFemina, P. C., Dixon, T. H., & Strauch, W. (2002). Bookshelf faulting in Nicaragua. *Geology*, *30*(8), 751–754.

Larson, K. M., Lowry, A. R., Kostoglodov, V., Hutton, W., Sánchez, O., Hudnut, K., & Suárez, G. (2004). Crustal deformation measurements in Guerrero, Mexico. *Journal of Geophysical Research*, *109*, B04409. https://doi.org/10.1029/2003JB002843

Lyard, F., Lefevre, F., Letellier, T., & Francis, O. (2006). Modeling the global ocean tides: Modern insights from FES2004. *Ocean Dynamics*, *56*(5–6), 394–415.

Maerten, F., Resor, P., Pollard, D., & Maerten, L. (2005). Inverting for slip on three-dimensional fault surfaces using angular dislocations. *Bulletin of the Seismological Society of America*, *95*(5), 1654–1665.

Malservisi, R., Schwartz, S. Y., Voss, N., Protti, M., Gonzalez, V., Dixon, T. H., et al. (2015). Multiscale postseismic behavior on a megathrust: The 2012 Nicoya earthquake, Costa Rica. *Geochemistry, Geophysics, Geosystems*, *16*, 1848–1864. https://doi.org/10.1002/2015GC005794

McCaffrey, R. (2007). The next great earthquake. *Science*, *315*(5819), 1675–1676. https://doi.org/10.1126/science.1140173

McCormack, K., Hesse, M. A., Dixon, T., & Malservisi, R. (2020). Modeling the contribution of poroelastic deformation to postseismic geodetic signals. *Geophysical Research Letters*, *47*, e2020GL086945. https://doi.org/10.1029/2020GL086945

Meade, B. J. (2007). Algorithms for the calculation of exact displacements, strains, and stresses for triangular dislocation elements in a uniform elastic half space. *Computers & Geosciences*, *33*(8), 1064–1075. https://doi.org/10.1016/j.cageo.2006.12.003

Norabuena, E., Dixon, T. H., Schwartz, S., DeShon, H., Newman, A., Protti, M., et al. (2004). Geodetic and seismic constraints on some seismogenic zone processes in Costa Rica. *Journal of Geophysical Research*, *109*, B11403. https://doi.org/10.1029/2003JB002931

Obara, K., Hirose, H., Yamamizu, F., & Kasahara, K. (2004). Episodic slow slip events accompanied by non-volcanic tremors in southwest Japan subduction zone. *Geophysical Research Letters*, *31*, L23602. https://doi.org/10.1029/2004GL020848

Ohta, Y., Freymueller, J. T., Hreinsdóttir, S., & Suito, H. (2006). A large slow slip event and the depth of the seismogenic zone in the south central Alaska subduction zone. *Earth and Planetary Science Letters*, *247*(1–2), 108–116.

Outerbridge, K. C., Dixon, T. H., Schwartz, S. Y., Walter, J. I., Protti, M., Gonzalez, V., et al. (2010). A tremor and slip event on the Cocos-Caribbean subduction zone as measured by a global positioning system (GPS) and seismic network on the Nicoya Peninsula, Costa Rica. *Journal of Geophysical Research*, *115*, B10408. https://doi.org/10.1029/2009JB006845

Protti, M., González, V., Newman, A. V., Dixon, T. H., Schwartz, S. Y., Marshall, J. S., et al. (2014). Nicoya earthquake rupture anticipated by geodetic measurement of the locked plate interface. *Nature Geoscience*, *7*(2), 117–121.

Protti, M., McNally, K., Pacheco, J., Gonzalez, V., Montero, C., Segura, J., et al. (1995). The March 25, 1990 (M_w = 7.0, ML = 6.8), earthquake at the entrance of the Nicoya Gulf, Costa Rica: Its prior activity, foreshocks, aftershocks, and triggered seismicity. *Journal of Geophysical Research*, *100*(B10), 20,345–20,358.

Rebischung, P., Altamimi, Z., Ray, J., & Garayt, B. (2016). The IGS contribution to ITRF2014. *Journal of Geodesy*, *90*(7), 611–630.

Reid, H. F. (1910). *The Mechanics of the Earthquake, the California Earthquake of April 18, 1906, Report of the State Investigation Commission* (Vol. 2). Washington, D.C: Carnegie Institution of Washington.

Rolandone, F., Nocquet, J. M., Mothes, P. A., Jarrin, P., Vallée, M., Cubas, N., et al. (2018). Areas prone to slow slip events impede earthquake rupture propagation and promote afterslip. *Science Advances*, *4*(1), eaao6596. https://doi.org/10.1126/sciadv.aao6596

Saffer, D. M., & Wallace, L. M. (2015). The frictional, hydrologic, metamorphic and thermal habitat of shallow slow earthquakes. *Nature Geoscience*, *8*(8), 594–600.

Salditch, L., Stein, S., Neely, J., Spencer, B. D., Brooks, E. M., Agnon, A., & Liu, M. (2020). Earthquake supercycles and long-term fault memory. *Tectonophysics*, *774*, 228–289.

Schwartz, S. Y., & Rokosky, J. M. (2007). Slow slip events and seismic tremor at circum-Pacific subduction zones. *Reviews of Geophysics*, *45*, RG3004. https://doi.org/10.1029/2006RG000208

Segall, P., & Bradley, A. M. (2012). Slow-slip evolves into megathrust earthquakes in 2D numerical simulations. *Geophysical Research Letters*, *39*, L18308. https://doi.org/10.1029/2012GL052811

Uchida, N., Iinuma, T., Nadeau, R. M., Bürgmann, R., & Hino, R. (2016). Periodic slow slip triggers megathrust zone earthquakes in northeastern Japan. *Science*, *351*(6272), 488–492. https://doi.org/10.1126/science.aad3108

Voss, N., Dixon, T. H., Liu, Z., Malservisi, R., Protti, M., & Schwartz, S. (2018). Do slow slip events trigger large and great megathrust earthquakes? *Science Advances*, *4*(10), eaat8472. https://doi.org/10.1126/sciadv.aat8472

Voss, N. K., Malservisi, R., Dixon, T. H., & Protti, M. (2017). Slow slip events in the early part of the earthquake cycle. *Journal of Geophysical Research: Solid Earth*, *122*, 6773–6786. https://doi.org/10.1002/2016JB013741

Wallace, L. M., Hreinsdóttir, S., Ellis, S., Hamling, I., D'Anastasio, E., & Denys, P. (2018). Triggered slow slip and afterslip on the southern Hikurangi subduction zone following the Kaikōura earthquake. *Geophysical Research Letters*, *45*, 4710–4718. https://doi.org/10.1002/2018GL077385

Walter, J. I., Schwartz, S. Y., Protti, J. M., & Gonzalez, V. (2011). Persistent tremor within the northern Costa Rica seismogenic zone. *Geophysical Research Letters*, *38*, L01307. https://doi.org/10.1029/2010GL045586

Walwer, D., Calais, E., & Ghil, M. (2016). Data-adaptive detection of transient deformation in geodetic networks. *Journal of Geophysical Research: Solid Earth*, *121*, 2129–2152. https://doi.org/10.1002/2015JB012424

Wang, G., Liu, H., Mattioli, G. S., Miller, M. M., Feaux, K., & Braun, J. (2019). CARIB18: A stable geodetic reference frame for geological hazard monitoring in the Caribbean region. *Remote Sensing*, *11*(6), 680. https://doi.org/10.3390/rs11060680

Yue, H., Lay, T., Schwartz, S. Y., Rivera, L., Protti, M., Dixon, T. H., et al. (2013). The 5 September 2012 Nicoya, Costa Rica M_w 7.6 earthquake rupture process from joint inversion of high-rate GPS, strong-motion, and teleseismic *P* wave data and its relationship to adjacent plate boundary interface properties. *Journal of Geophysical Research: Solid Earth*, *118*, 5453–5466. https://doi.org/10.1002/jgrb.50379

Zumberge, J. F., Heflin, M. B., Jefferson, D. C., Watkins, M. M., & Webb, F. H. (1997). Precise point positioning for the efficient and robust analysis of GPS data from large networks. *Journal of Geophysical Research*, *102*(B3), 5005–5017.

Zwillinger, D., & Kokoska, S. (1999). *CRC Standard Probability and Statistics Tables and Formulae* (pp. 346–350). Boca Raton, Fla: CRC Press.